Journal of Building Engineering 34 (2021) 101875

Contents lists available at ScienceDirect

Journal of Building Engineering

journal homepage: http://www.elsevier.com/locate/jobe

Finite element analysis for progressive collapse potential of precast concrete beam-to-column connections strengthened with steel plates

Hussein M. Elsanadedy [1,*], Yousef A. Al-Salloum, Mohammed A. Alrubaidi, Tarek H. Almusallam, Husain Abbas

Chair of Research and Studies in Strengthening and Rehabilitation of Structures, Dept. of Civil Eng., College of Eng., King Saud University, P.O. Box 800, Riyadh 11421, Saudi Arabia

ARTICLE INFO

Keywords:
Strengthening
Steel plates
Progressive collapse
Precast beam-column connection
Column-removal scenario
Finite element model

ABSTRACT

Compared to monolithic reinforced concrete (RC) buildings, precast RC buildings are more prone to the risk of progressive collapse. Therefore, there is a need for efficient methods to strengthen beam-column joints in existing precast structures for mitigating the progressive collapse. This paper studies numerically using the finite element (FE) method the risk of progressive collapse of precast concrete beam-to-column connections rehabilitated with steel plates under middle column-loss event. Nonlinear FE models were established with the help of LS-DYNA software for predicting the response of both unstrengthened and strengthened precast RC single story two-bay frames under middle column-loss event. The developed FE models consider material nonlinearity – including strain-rate effect – for concrete, steel rebars, rubber pads and steel plates; in addition to contact behavior between different members in the joint region. The models were validated using the data of three half-scale frames tested under middle column-loss event. Specimens involved: one control unstrengthened precast RC frame, one monolithic assembly with continuous beam rebars, and another precast assembly alike the control frame but rehabilitated utilizing steel plates in joint region. The calibrated FE modeling was employed for parametric studies of practical interest wherein the influence of steel plate parameters was studied.

1. Introduction

The last few decades have witnessed an upsurge in the construction of precast reinforced concrete (RC) framed buildings around the globe due to the inherent advantages of precast system over the conventional cast-in-situ RC frame construction. Besides better quality control, the precast construction leads to the reduction in formwork, scaffolding, skilled labor, material waste, and construction duration.

Shear behavior of precast RC shear walls with different connection designs has been investigated in the literature. Smith et al. [1] studied experimentally the seismic performance of three different designs of precast RC shear wall specimens. Test walls included two hybrid specimens and a third precast wall designed to emulate cast-in-situ monolithic RC shear walls. The first two walls used hybrid reinforcement (mild steel rebars and unbonded posttensioning strands) for lateral load resistance, while the emulative wall utilized only mild steel rebars. For the emulative wall and one of the hybrid specimens, wall-to-foundation connection comprised of Type II mechanical splices of steel rebars, whereas the other hybrid wall utilized continuous rebars grouted into the foundation. Test results revealed the potential for the use of precast RC shear walls in seismic areas, while also pointing out the importance of detailing at wall-to-footing joint. In another study, Chen et al. [2] investigated experimentally the shear resistance of precast RC shear walls with new bundled connections. A new assembling means for lower and upper wall panels is suggested, while vertical steel rebars are assembled into bundles and then connected in developed holes. In order to assess the shear resistance of such a new connection, three precast shear wall specimens with different horizontal steel rebars have been tested under monotonic lateral loading combined with constant axial compression. Tests revealed the reliability of the innovative connection design with no pulling out or significant slippage of rebars.

The RC framed buildings are highly vulnerable to progressive collapse initiated by the collapse of one or more columns under an extreme event such as the exposure to the blast generated waves. The

* Corresponding author.
E-mail address: helsanadedy@ksu.edu.sa (H.M. Elsanadedy).
[1] On leave from Helwan University, Cairo, Egypt.

https://doi.org/10.1016/j.jobe.2020.101875
Received 3 April 2020; Received in revised form 24 August 2020; Accepted 6 October 2020
Available online 10 October 2020

Table 1
Dimensions and reinforcement details of prototype frame and test specimens*.

Type	Beam			Column			Corbel		Thickness of steel plates (mm)
	Dimensions (mm) ($b \times h \times L$)	Longitudinal bottom (or top) steel	Stirrups	Dimensions (mm) ($b \times h \times H$)	Longitudinal steel	Stirrups	Dimensions (mm) ($b \times h \times L$)	Longitudinal bottom (or top) steel	
Prototype	700 × 700 × 5240	7-D25	5-legged D12@200 mm o.c	700 × 700 × 3500	8-D32	D12@100 mm o.c	700 × 500 × 400	7-D25	20
Specimen PC-C	350 × 350 × 2620	4-D16	2-legged D8@100 mm o.c	350 × 350 × 1750	8-D16	D8@100 mm o.c	350 × 250 × 200	4-D16	–
Specimen MC-SMF	350 × 350 × 2650	4-D16	2-legged D8@100 mm o.c	350 × 350 × 1750	8-D16	D8@100 mm o.c	–	–	–
Specimen PC-S	350 × 350 × 2620	4-D16	2-legged D8@100 mm o.c	350 × 350 × 1750	8-D16	D8@100 mm o.c	350 × 250 × 200	4-D16	10

*b = width of beam (column or corbel) section; h = depth of beam (column or corbel) section; L = beam (or corbel) net span; H = column height.

progressive collapse starts with some localized damage of a structural member and propagates to the adjoining structural elements progressively spreading over a larger area leading to the partial or total collapse of the structure. On the other hand, the precast RC framed buildings are more prone to the progressive collapse due the lack of redundancy and hence the lack of availability of alternate load paths. It is thus prudent to upgrade the existing precast RC framed buildings for resisting progressive collapse and this requires efficient retrofitting methods.

The load-displacement response of different designs of precast concrete beam-to-column connections has been studied by several researchers [3–9] and the response was compared with the cast-in-situ connections. The strengthening of these structures often requires analysis for feasible prestress modes [10] and collapse loads of multi-span masonry arch structures [11].

Many researchers [12–22] have studied the progressive collapse risk of RC buildings by removing one of the columns and testing the frame and applying load at the upper joint of the removed column. This method helps in assessing the availability of alternate load paths and its consequent effect on the propagation of damage to adjoining structural members.

Seismic collapse analysis of high-rise RC buildings has been also studied in the literature. Bai et al. [23] investigated numerically the seismic-induced damages and collapse of typical high-rise RC building frames involving strength degradation effects. Finite element analysis was conducted for the building using fiber discretization method. In this analysis, nonlinear effects such as concrete confinement, concrete crushing, and buckling of steel rebars were considered. It was concluded that the strength degradation effect in RC members with small transverse reinforcement ratio amplify the seismic responses in high-rise RC moment-resisting frames when the intensity of ground motions surpasses the design level.

The strengthening of deficient RC beam-column joints of monolithic frames has been widely studied by employing conventional and non-conventional methods using fiber reinforced polymer (FRP) and fabric reinforced cementitious mortar (FRCM). These methods include jackets of concrete and steel [24,25], wrapping with FRP laminates [26–28], and FRCM retrofitting [29]. Nevertheless, upgrading of beam-column joints of an existing precast RC frame is a great challenge due to the associated practical problems. Da Fonseca et al. [30] strengthened a single bay precast RC frame with the help of near surface mounted (NSM) carbon FRP (CFRP) sheets. The frame was tested till failure. The retrofitted beam-column joints were found to behave as semi-rigid joints, which resulted in considerably reduced deflections.

Pan et al. [31] investigated experimentally two half-scale precast RC framed sub-assemblages under a pushdown loading regime simulating column-loss scenarios in real progressive collapse occasions. One of the frames was upgraded using CFRP laminates on the side faces of the beam. The central portion of the laminates were anchored using hybrid FRP (HFRP) anchors. The strengthening was proven to be effective up to the early catenary action (CA) stage (corresponds to maximum push-down displacement of $0.2L$ where L = beam span). Nevertheless, at the deformation levels exceeding 20% of the span, rupture of CFRP laminate occurred and the CFRP laminates no longer contributed to the capacity. No shearing failure developed in the HFRP anchors, which proves the efficiency of the anchorage method.

An experimental program was carried out by Al-Salloum et al. [32] to strengthen beam-column connections in existing single story, two-bay precast concrete frames with the help of steel plates for progressive collapse mitigation. Three half-scale frames were prepared. The first frame was unstrengthened control precast specimen simulating most common precast RC beam-column joints in Saudi Arabia. The second frame was monolithic having continuous longitudinal rebars in beams; whereas the third frame was the strengthened precast frame. For simulating the progressive collapse, the assemblies were tested after removing the support of the middle column and applying load at its upper joint. Behavior of both unstrengthened and strengthened precast

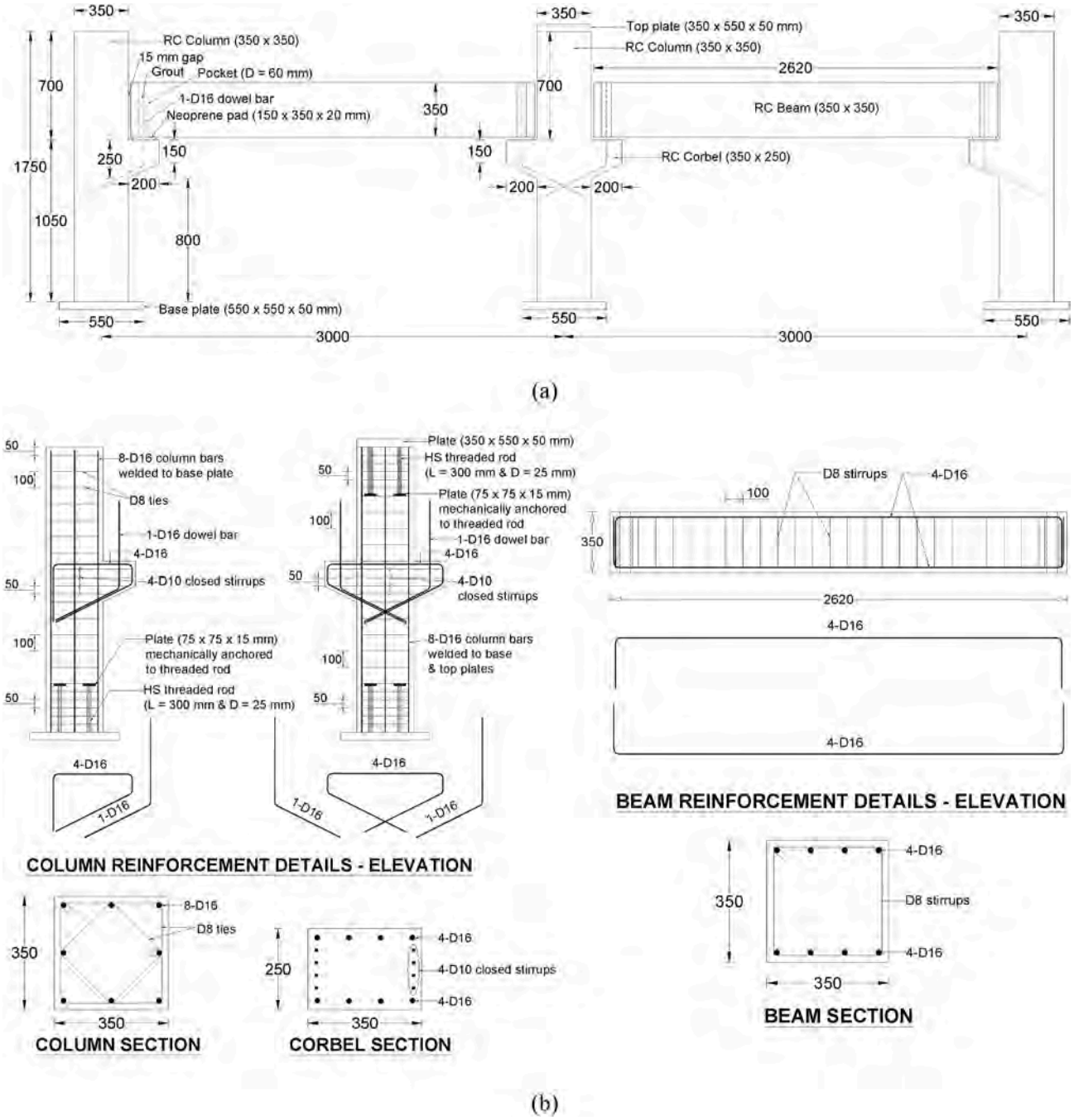

Fig. 1. Details of precast specimen PC-C as taken from Ref. [32] (Note: All dimensions are in mm): (a) Test specimen; (b) Reinforcement details.

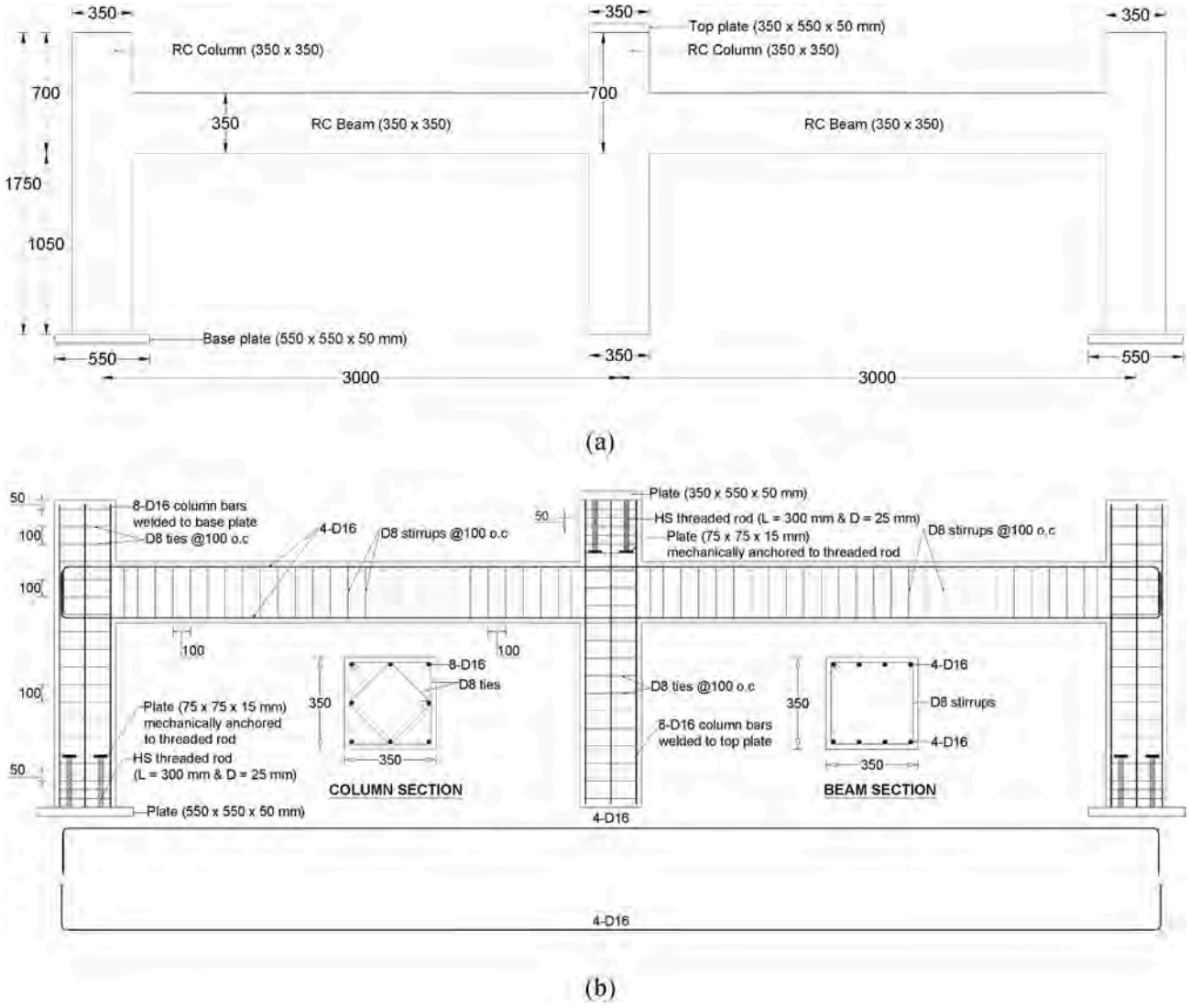

Fig. 2. Details of monolithic specimen MC-SMF as taken from Ref. [32] (Note: All dimensions are in mm): (a) Test specimen; (b) Reinforcement details.

frames was compared with the monolithic test assembly.

The aim of this paper is to study numerically, by employing the finite element (FE) method, the progressive collapse potential in precast RC beam-to-column connections upgraded with steel plates under middle column-loss scenario. Nonlinear FE models were developed with the help of LS-DYNA software [33] for predicting the response of both unstrengthened and strengthened precast concrete 2D frames for column-removal events. The developed FE models considered material nonlinearity with strain-rate effect in addition to the contact behavior between different members at the joint. The test results of Al-Salloum et al. [32] were used for validating the numerical model. The validated FE modeling was employed for conducting parametric studies of practical interest.

2. Experimental study

For achieving the aim of this study, experimental test results have to be accessed and employed for the calibration of FE models. For this purpose, three 2D assemblies (PC–C, MC-SMF and PC-S), which have been tested previously by Al-Salloum et al. [32] for middle column-removal event, have been employed. The test frames – in terms of geometric dimensions and reinforcement detailing – were designed to be half-scale of a two-bay prototype perimeter frame that was assumed to be part of an existing precast RC building located in Saudi Arabia. Table 1 presents the dimensions and reinforcement detailing for both the prototype frame and the specimens. It is noted from Table 1 that dimensions of test frames are one-half of the prototype frame. Steel plates of specimen PC-S as well as longitudinal steel rebars of beams, corbels, and columns of all test frames were selected to give approximately the same reinforcement ratio as the prototype frame. However, transverse reinforcement of members of test specimens was designed to have nearly the same volumetric ratio as the prototype frame. The first specimen PC-C (Fig. 1) was a precast RC frame, which represents the most prevalent type of beam-column joints in many parts of the world including Saudi Arabia. The preparation of the frame involved casting of the individual members and then assembling the members, as done in practice. The second test specimen MC-SMF was a monolithic frame (Fig. 2) in which the longitudinal rebars in the beams were continuous over the middle column. The third test specimen PC-S was a strengthened precast frame (Figs. 1 and 3). This frame was the same as the control one but its beam-column joints were upgraded using steel plates, which were bolted in the joint region. The member sizes and detailing of reinforcement of the two test frames PC-C and PC-S were same. The beam and column cross-sections were square of 350 mm size. The corbel section was 350 × 250 mm. The column height up to the beam soffit was 1070 mm. The columns were resting on 500 mm high steel stubs thus making the total

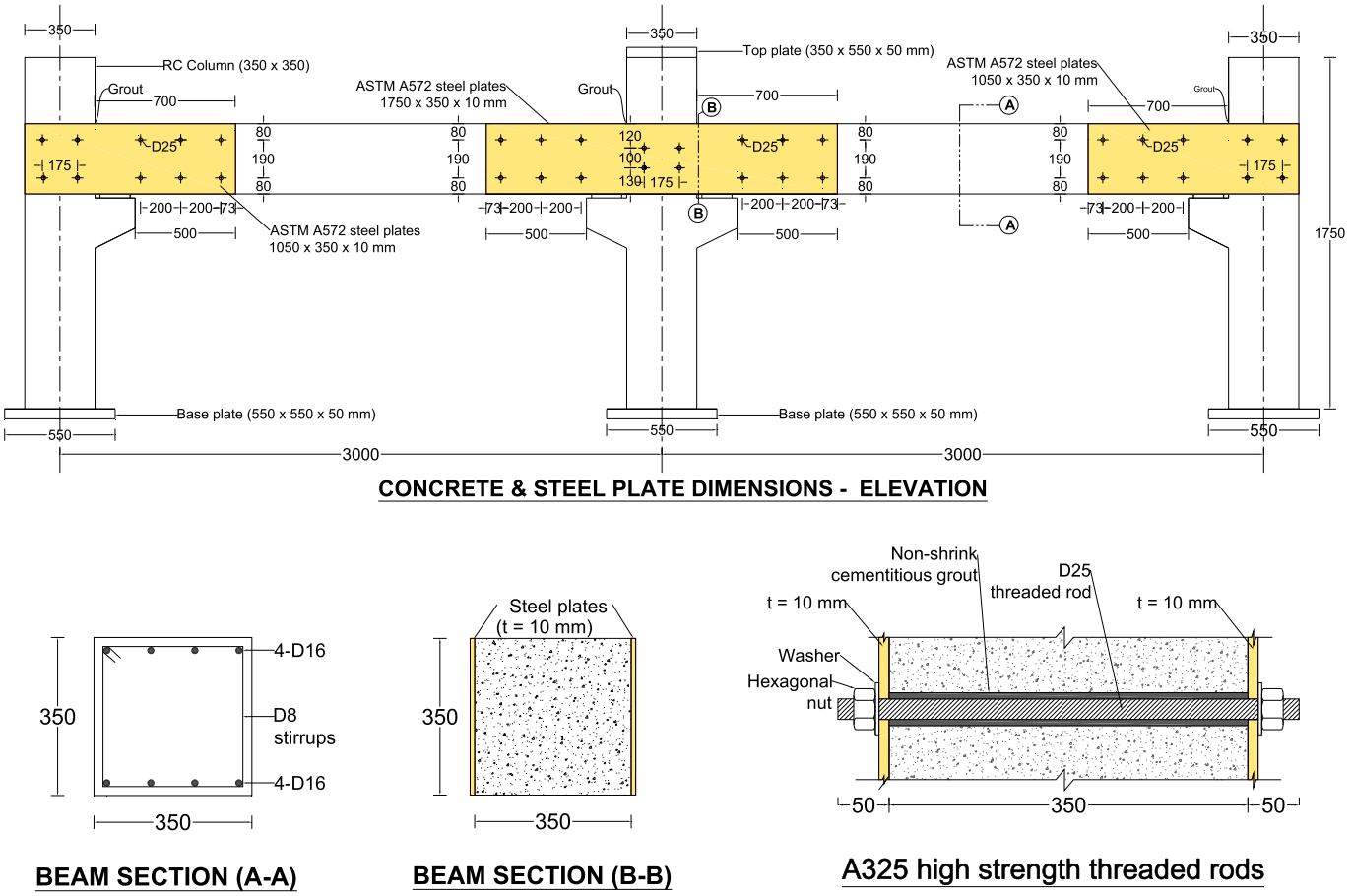

Fig. 3. Details of strengthened specimen PC-S as taken from Ref. [32] (Note: All dimensions are in mm).

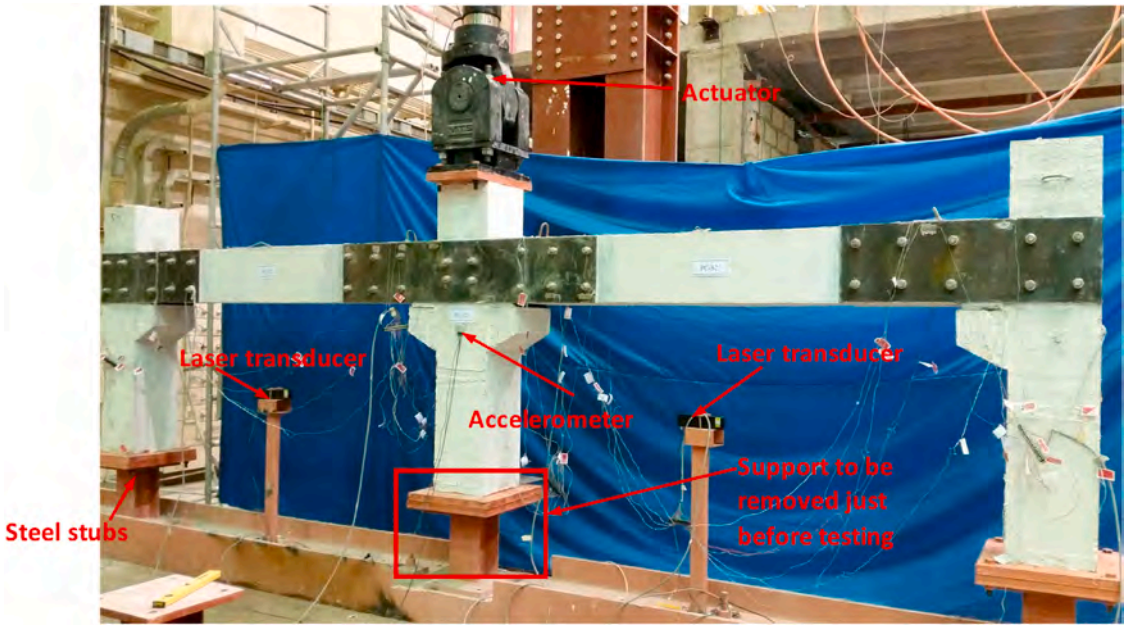

Fig. 4. Test setup and instrumentation layout for specimen PC-S.

Table 2
Material properties used in the FE modeling.

Concrete & cementitious grout						
Material model	Type 159 (MAT_CSCM_CONCRETE)					
Density (kg/m^3)	2320					
Uni-axial compressive strength (MPa)	37.3 for concrete & 60 for cementitious grout					
Steel rebars, threaded rods & plates	*D8*	*D10*	*D16*	*Threaded rods*	*A572 plates*	*A36 plates*
Material model	Type 24 (MAT_PIECEWISE_LINEAR_PLASTICITY)					
Density (kg/m^3)	7850					
Young's modulus (GPa)	200					
Poisson's ratio	0.3					
Strain rate parameter, C	250					
Strain rate parameter, *p*	1.6					
Yield stress (MPa)	525	489	526	350	408	248
Tangent modulus (MPa)	127	2127	1065	0	485	765
Plastic strain to failure (%)	19.7	11.6	11.7	19.8	19.7	19.8
Neoprene pads						
Material model	Type 77 (MAT_HYPERELASTIC_RUBBER)					
Density (kg/m^3)	1100					
Poisson's ratio	0.499					
Shear modulus (MPa)	1.38					
Limit stress (MPa)	5.52×10^{-3}					
Constant C_{10}	0.55					
Constant C_{01}	0					
Constant C_{11}	0					
Constant C_{20}	−0.05					
Constant C_{02}	0					
Constant C_{30}	0.95					
Steel stubs at base of columns						
Material model	Type 1 (MAT_ELASTIC)					
Density (kg/m^3)	7850					
Young's modulus (GPa)	200					
Poisson's ratio	0.3					

height of column as 1570 mm (measured up to the beam soffit). The steel stubs were attached to steel I-section, which was tightly anchored to the strong laboratory floor (Fig. 4). The beams were reinforced with 4-D16 mm longitudinal rebars provided at the top as well as the bottom face. The beam shear reinforcement was in the form of two legged stirrups of D8 mm rebars provided at a center-to-center spacing of 100 mm. The columns were reinforced with 8-D16 mm longitudinal rebars. The D8 mm rebars were used as ties, which were provided at a spacing that varied along the column height (Fig. 1). The beam-column joint consisted of a protruding D16 mm rebar cast with the corbel. During fabrication, the rebar was made to pass through D60 mm circular hole provided at the beam ends. A neoprene pad of 20 mm thickness was used to support the beam on the corbel. The beam hole with corbel rebar was subsequently grouted with the help of non-shrink cementitious mortar. The member sizes of test frame MC-SMF were the same as that of frame PC-C, except the absence of corbels. The detailing of reinforcement of specimen MC-SMF was also the same as frame PC-C (precast frame) except that the bottom and top longitudinal beam rebars were continuous over the middle column (Fig. 2).

The strengthening design of steel plates was performed to upgrade the shear and bending resistance of the precast frame to the level of monolithic frame MC-SMF approximately. The strain-rate effect on the material response was ignored and thus the nominal material properties were used in the design. The locally available ASTM A572 G50 steel was used in the design. Although the required thickness of steel plate was 5.8 mm, 10 mm thick steel plate was used due to the non-availability of lesser plate thickness. The lengths of 10 mm thick ASTM A572 G50 steel plates used for the strengthening of the interior and the exterior joints were 1750 and 1050 mm, respectively. The length of the plate was decided so as to maintain an extension of twice the beam depth beyond the face of the column (Fig. 3). The extension of the plate was sufficient to cover the plastic hinge zone, as required by the ACI code [34] for RC special moment frames. The depth of the plate was equal to the depth of the beam (= 350 mm). The steel plates were connected to the frame using high strength steel rods of 25 mm diameter (Fig. 3), which were designed for resisting shear. Before connecting steel plates, the surfaces of the contact zones were prepared by manual grinding and subsequent sandblasting. Although the steel plates were connected to the frame using steel rods, epoxy mortar was employed for bonding of the steel plates with concrete surface. The non-shrink cementitious mortar was grouted in the gaps at beam-column interfaces and hollow pockets at the beam ends.

The specimens were cast using ready-mix concrete. The standard cylinders prepared at the time of casting were tested in compression on the test date as per relevant ASTM standard [35] and the compressive strength was found to be 37.3 MPa. The steel rebars were tested in tension as per relevant ASTM standard [36] and the test results are given in Table 2. The coupons of steel plates were tested as per relevant ASTM standard [37] and the test results are also provided in Table 2.

It is worth mentioning that column-loss event in progressive collapse problems may be dealt with as an extreme scenario of unexpected loadings such as explosions and impact. Loss of columns is therefore

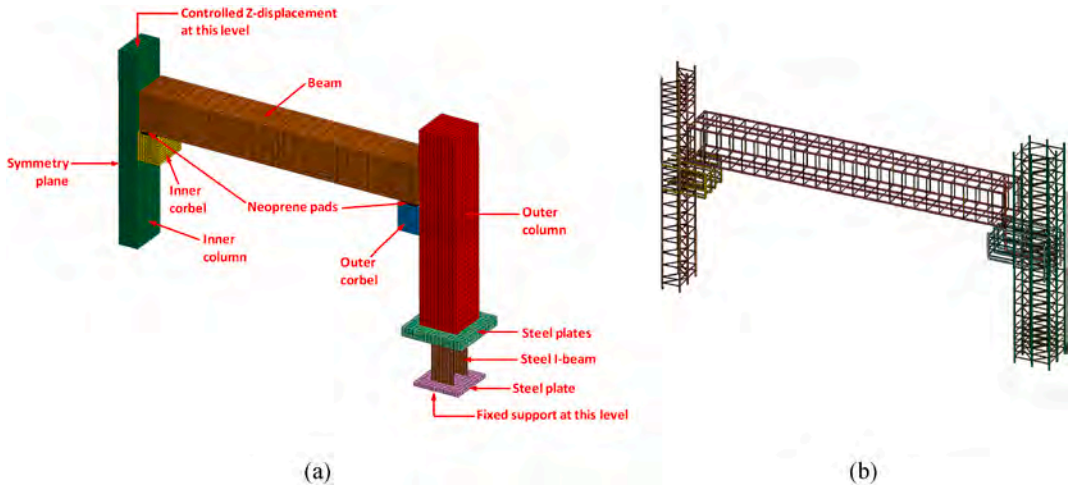

Fig. 5. FE model for one-half of specimen PC-C: (a) FE mesh; (b) FE model of steel reinforcement.

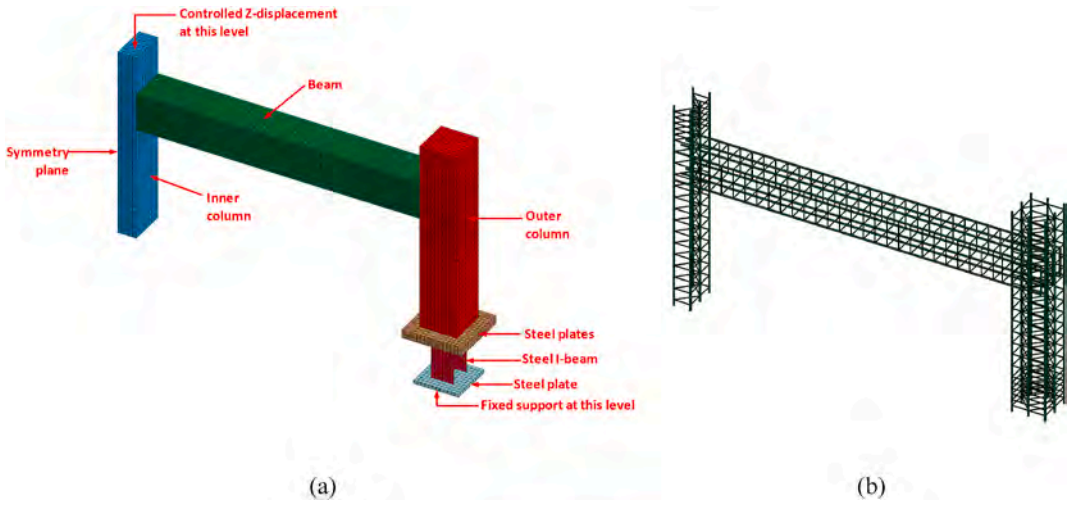

Fig. 6. FE model for one-half of specimen MC-SMF: (a) FE mesh; (b) FE model of steel reinforcement.

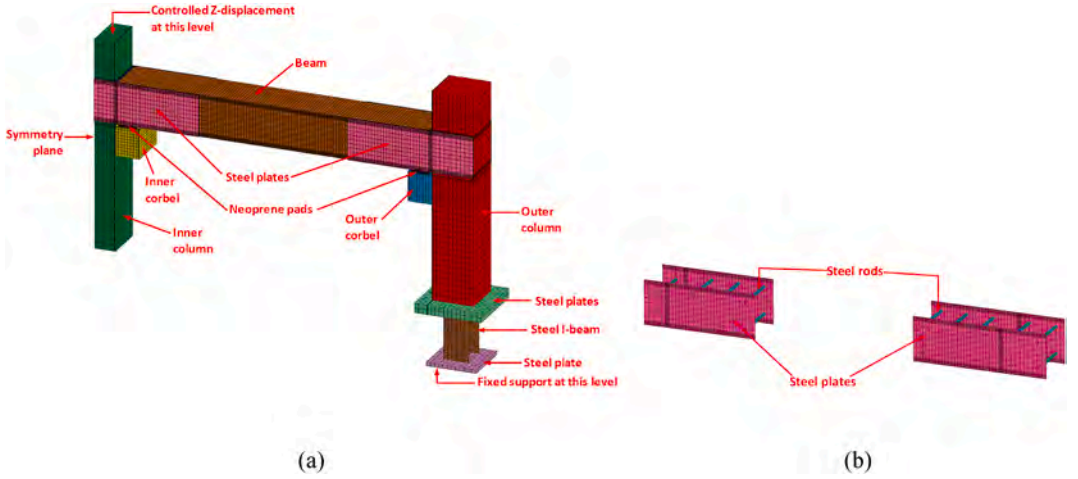

Fig. 7. FE model for one-half of specimen PC-S: (a) FE mesh; (b) FE model of steel plates with rods.

sudden and occurs in a very short duration, which will bring the problem into the dynamic domain with high strain-rate effects. This sudden column-loss scenario was simulated in the experiments by releasing the support of the middle column and applying displacement-controlled load on that column using a high speed actuator at a rate of 100 mm/s (Fig. 4). However, the high speed in real progressive collapse events could not be accommodated in the experiments due to the limits of the used actuator. The loading rate adopted (i.e., 100 mm/s) was similar to quasi-static type testing. Thus, the inertial effects in experiments were of smaller scale than expected in a column-removal scenario. However, the increase in stresses due to the inertial forces is partly compensated by the enhanced material strength due to strain-rate effect.

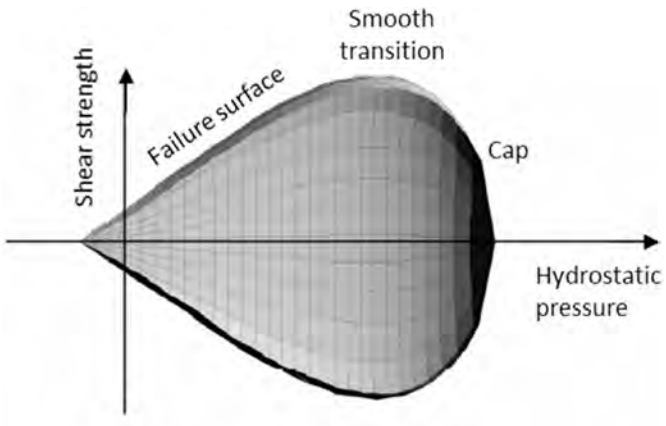

Fig. 8. General shape of the concrete model yield surface in two-dimensions.

3. Finite element modeling

The test frames were modeled using the commercial FE package LS-DYNA [33]. Only one-half of the test frame was simulated due to its symmetry.

3.1. Geometry of FE model

Figs. 5–7 present the FE mesh for one-half of the test frames PC-C, MC-SMF and PC-S, respectively. Solid reduced integration elements of eight nodes were used to model concrete volume of beams, columns and corbels, in addition to the neoprene pads of precast frames PC-C and PC-S. The element has three translation degrees of freedom at each node. As seen in Figs. 5(b) and 6(b), beam elements of two nodes were employed to model both longitudinal and transverse reinforcement of test frames. The element has six degrees of freedom at each node: three translations and three rotations about Cartesian axes. As illustrated in Fig. 7(b), steel plates of test frame PC-S were simulated with the help of four-node shell

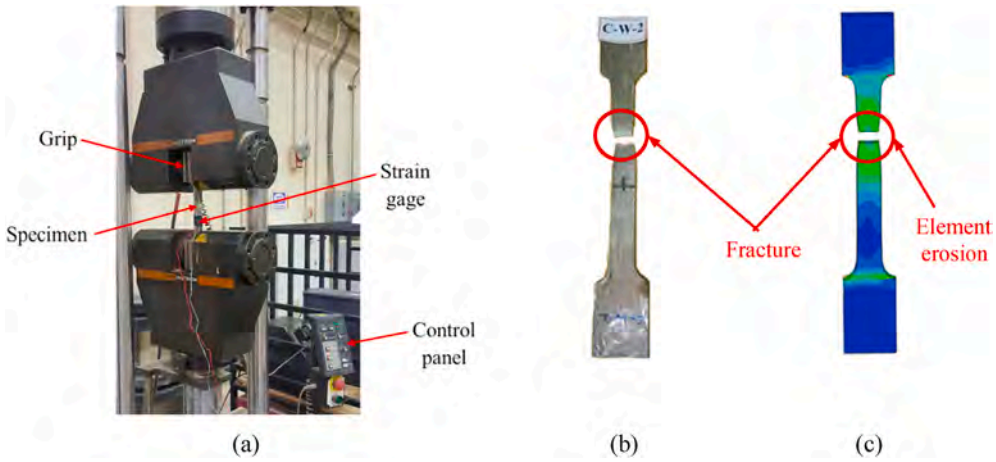

Fig. 9. Standard tensile coupon for A572 G50 steel plates: (a) Tensile test; (b) Experimental mode of failure; (c) FE mode of failure.

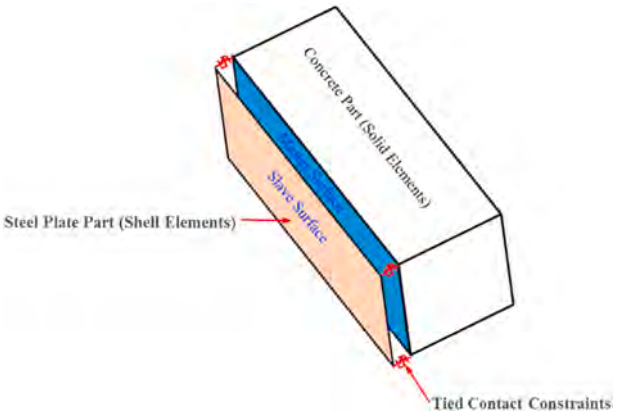

Fig. 10. Tiebreak surface-to-surface contact of steel plates-to-concrete interface.

elements of Belytschko-Tsay formulation [38]; whereas, the threaded rods were simulated using two-node beam elements. The shell element has both bending and membrane capabilities. Both in-plane and normal loads are permitted. The element has six degrees of freedom at each node: three translations and three rotations about Cartesian axes. For modeling of the I-shaped steel stubs at the base of outer columns, eight-node solid elements were employed to simulate steel plates; while four-node shell elements were used to model the I-beams, as seen in Figs. 5(a), 6(a) and 7(a). In all specimens, size of beam, solid and shell elements varied from 2.5 to 50 mm. Mesh sensitivity analysis was carried out and it was realized that more refinement of the mesh size would have slight influence on the FE results; however, it may increase the solution time substantially.

3.2. Material models

Table 2 summarizes all material properties employed in the FE analysis. Rate-dependent material models were employed to account for the dynamic nature of the applied load in the tests (rate of loading was 100 mm/s). Among various concrete models available in LS-DYNA, material model type 159 (continuous surface cap model) was employed for concrete of beams, columns and corbels. The reasons for this selection are that (i) it has several options such as modeling of existing pre-damage effects, element erosion and viscoplastic strain-rate effects; (ii) it has simple input parameters for concrete; and (iii) it has been used successfully by authors in numerical modeling of various RC members with static and dynamic loading applications [7,39–44]. Fig. 8 presents the general shape of concrete model yield surface in two dimensions. This model has a smooth intersection between the hardening cap and the shear yield surface as illustrated in Fig. 8. The initial damage surface coincides with the yield surface. The yield surface is formulated in terms of three stress invariants. Concrete cracking is treated using the conventional smeared crack approach.

For concrete material model type 159, the viscoplastic rate effects are incorporated. At each time step, the stress is updated from the strain-rate increments and the time step via an incremental form of Hooke's Law (an elastic increment). This updated stress is called the trial elastic stress and is denoted σ_{ij}^{T}. If the trial elastic stress state lies on or inside the yield surface, the behavior is elastic, and the plasticity algorithm is bypassed. If the trial elastic stress state lies outside the yield surface, the behavior is elastic-plastic (with possible damage, hardening, and rate effects), and the plasticity algorithm returns the stress state to the yield surface. This elastic-plastic stress is called the inviscid stress, and is denoted σ_{ij}^{p}. At each time step, the viscoplastic stress (with rate effects) σ_{ij}^{vp}, is given by

$$\sigma_{ij}^{vp} = (1-\gamma)\sigma_{ij}^{T} + \gamma\sigma_{ij}^{p} \tag{1}$$

with

$$\gamma = \frac{\Delta t/\eta}{1+\Delta t/\eta} \tag{2}$$

where Δt is the time step and η is the effective fluidity coefficient, which is internally calculated in the software using the strain rate. More details of this material model can be found in Refs. [33,45].

The erosion option introduces a means of adding failure to the material models. By adding this feature in the model, the eroded element is physically isolated from the rest of the FE mesh. In the FE analysis, the erosion option is associated with the material models. For material model type 159, solid concrete elements were eroded when the maximum principal concrete strain reached 5%. This erosion limit was recommended by Murray et al. [45]. It was also supported by authors in many studies that included FE modeling of RC members [7,39–44], by giving numerical results – in terms of failure modes and load-displacement characteristics – that match well with the experimental results.

Material model type 24 (piecewise linear plasticity model) [33] was used for transverse and longitudinal steel rebars of columns, corbels and beams, in addition to steel plates and rods of strengthened frame PC-S. For this material model, the stress-strain behavior was treated by a bilinear stress-strain curve by defining the tangent modulus (Table 2), which is used to compute the steel stress in the post-yield stage. The following Cowper-Symonds relationship was employed to account for

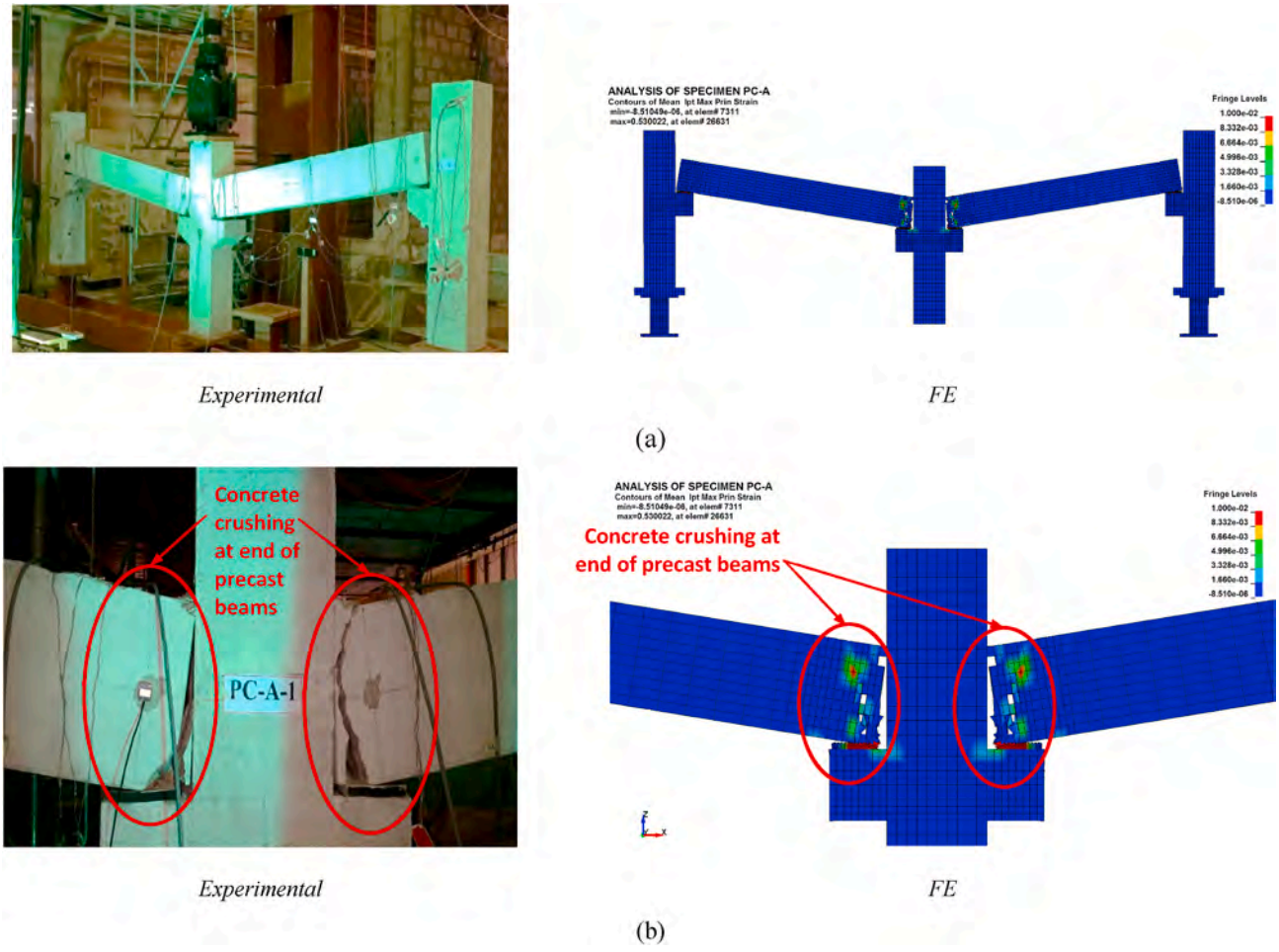

Fig. 11. Comparison of experimental and FE mode of failure of specimen PC-C: (a) Final deformed shape; (b) Failure of middle joint.

yield stress increase owing to strain-rate effect.

$$(DIF)_{\sigma_y} = 1 + \left(\frac{\dot{\varepsilon}}{C}\right)^{1/p} (\text{Units of } \dot{\varepsilon} : \text{s}^{-1}) \quad (3)$$

where $(DIF)_{\sigma_y}$ = dynamic increase factor of yield stress due to strain-rate effect, $\dot{\varepsilon}$ = strain rate, C = model parameter taken as 250, and p = model parameter taken as 1.6. The dynamic increase factor is used to scale the yield stress of steel elements as per the following equation:

$$\sigma_y = (DIF)_{\sigma_y} . \sigma_y^s \quad (4)$$

where σ_y = yield stress of steel element with strain-rate effect included; σ_y^s = static yield stress of steel element.

For estimation of input parameters for material model type 24 (listed in Table 2), tensile tests were conducted on standard steel coupons (steel rebars and plates) as per relevant standards in Refs. [36,37]. The output of each tensile test is the engineering stress-strain curve. FE models were created in LS-DYNA [33] for the tensile test of steel coupons, using the actual dimensions of the coupon specimens. For beam and shell elements representing steel rebars and plates, respectively, the engineering stress-strain curve in the FE models cannot be converted directly to the true stress versus effective plastic strain curve because the cross-sectional area of the element remains constant (true stress is equal to engineering stress in this case). In the FE models, the element size was calibrated by iterative analysis. The size of the FE mesh was adjusted until quantitative agreement of the measured and calculated engineering stress-strain behavior was attained for the coupon specimens. The experimentally observed steel fracture was simulated by element erosion using the plastic strain to failure. As an example, Fig. 9 shows comparison between the experimental and FE failure modes for the standard coupon test of A572 G50 steel plates used in current study. Good agreement was noticed between the experimental and FE results. This confirms the aptness of both element size and input material parameters in capturing steel fracture via element erosion. Thus, the calibrated element size has been used in the 3D FE modeling of the frame assemblies, especially at critical locations of plastic hinges. For the I-shaped steel stubs at the base of outer columns, the linear elastic material model type 1 was used for both plates and steel I-beams (see Table 2).

For precast frames PC-C and PC-S, material model type 77 (hyperelastic rubber material model) [33,46] was used for solid elements of the neoprene pads. In this model, the principal Kirchoff stress components

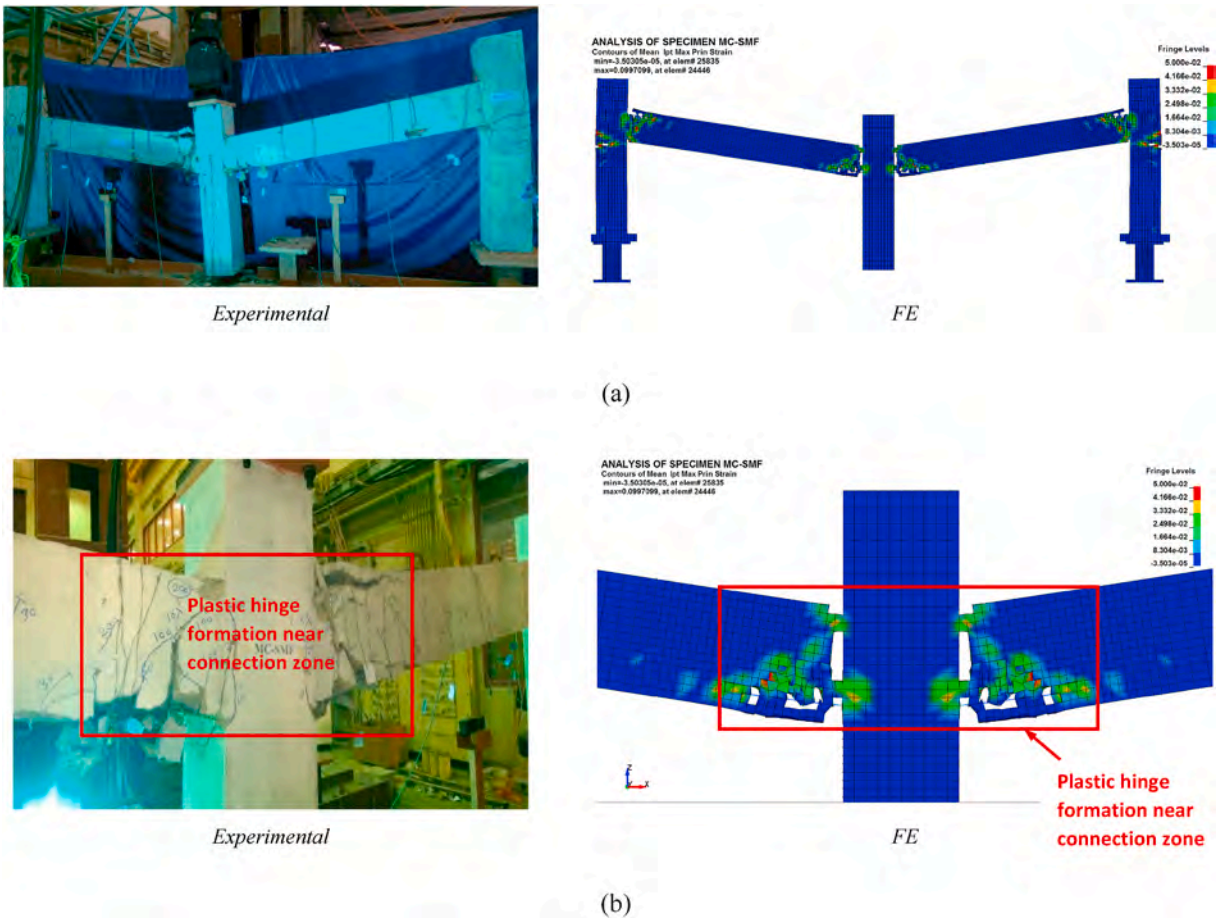

Fig. 12. Comparison of experimental and FE mode of failure of specimen MC-SMF: (a) Final deformed shape; (b) Failure of middle joint.

are given by

$$\tau_{ii}^{E} = \left(C_{10} + C_{11}W_2 + 2C_{20}W_1 + 3C_{30}W_1^2\right)W_{1i}^{'} + \left(C_{01} + C_{11}W_1 + 2C_{02}W_2\right)W_{2i}^{'} + KJ(J-1) \tag{5}$$

where C_{10}, C_{11}, C_{20}, C_{30}, C_{01} and C_{02} are material constants as given in Table 2; and W_1 & W_2 are strain energy functions given by

$$W_1 = I_1 I_3^{-1/3} - 3 \tag{6}$$

$$W_2 = I_2 I_3^{-2/3} - 3 \tag{7}$$

where I_1, I_2 and I_3 are the invariants of deformation tensor given in terms of the principal stretches λ_1, λ_2 and λ_3 from

$$I_1 = \lambda_1^2 + \lambda_2^2 + \lambda_3^2 \tag{8}$$

$$I_2 = \lambda_1^2\lambda_2^2 + \lambda_2^2\lambda_3^2 + \lambda_1^2\lambda_3^2 \tag{9}$$

$$I_3 = \lambda_1^2\lambda_2^2\lambda_3^2 \tag{10}$$

The strain energy derivatives $W_{1i}^{'}$ and $W_{2i}^{'}$ in Eq. (5) are given by

$$W_{1i}^{'} = \lambda_i \frac{\partial W_1}{\partial \lambda_i} = \left(2\lambda_i^2 - \frac{2}{3}I_1\right)I_3^{-1/3} \tag{11}$$

$$W_{2i}^{'} = \lambda_i \frac{\partial W_2}{\partial \lambda_i} = \left(2\lambda_i^2\left(I_1 - \lambda_i^2\right) - \frac{4}{3}I_2\right)I_3^{-2/3} \tag{12}$$

In Eq. (5), the parameter K is the bulk modulus and J is the relative volume change $= \lambda_1\lambda_2\lambda_3$.

3.3. Contact modeling

For all test assemblies, bond-slip behavior was not modeled between steel reinforcement rebars and surrounding concrete and perfect bond was assumed. In precast specimen PC-C, the 15 mm gap at beam-column interface was physically modeled by assigning two different parts for beam and column. Each part was separately meshed and an automatic surface-to-surface contact was assigned between the two parts. In this contact, the beam part was taken as master and the column part was assumed as slave. For contact definition, coefficient of friction has to be assigned between the master and slave parts. For beam-column interface, a coefficient of friction of 0.6 was assumed between the two concrete parts [34]. This coefficient of friction was assumed constant and was not dependent on the relative velocities of the two surfaces in contact. However, in strengthened precast specimen PC-S, the gap at beam-column interface was filled with cementitious grout. This gap was meshed using eight-node reduced integration solid elements, and full bond was modeled between elements of beam, column and the gap. In addition, for precast frames PC-C and PC-S, an automatic surface-to-surface contact was modeled between beam (assumed as master) and rubber pad (taken as slave), and between rubber pad (taken as master) and corbel (assumed as slave). Friction coefficient of 0.4 was taken between concrete parts and neoprene pads [47]. This friction coefficient was assumed constant and was not dependent on the relative velocities of the two surfaces in contact.

For strengthened frame PC-S, bond at steel plates-to-concrete interface was simulated utilizing the tiebreak surface-to-surface contact, as per the following bond strength failure criterion:

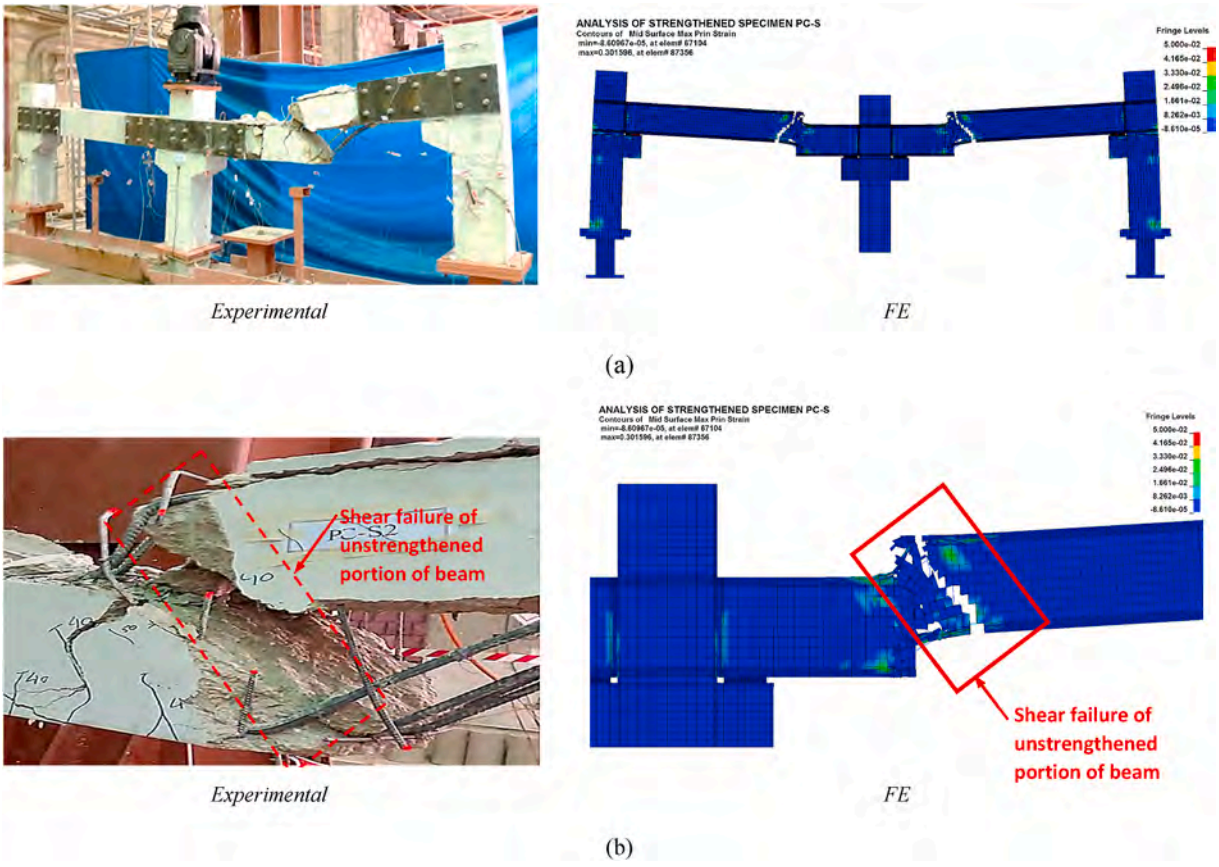

Fig. 13. Comparison of experimental and FE mode of failure of specimen PC-S: (a) Final deformed shape; (b) Close-up of beam shear failure.

$$\left(\frac{|\sigma_n|}{\sigma_{n,F}}\right)^2 + \left(\frac{|\sigma_s|}{\sigma_{s,F}}\right)^2 \geq 1 \tag{13}$$

where σ_n and σ_s are, in turn, the normal and shear stresses at contact surfaces. Yet, $\sigma_{n,F}$ and $\sigma_{s,F}$ are the normal and shear stresses at failure, respectively, calculated from Refs. [40,48]:

$$\sigma_{n,F} = 0.2\sqrt{f_c'}(\text{Units: MPa}) \tag{14}$$

$$\sigma_{s,F} = 0.62\sqrt{f_c'}(\text{Units: MPa}) \tag{15}$$

where f_c' is the specified concrete strength. In this contact, concrete surface was input as master and the steel plate was taken as slave as seen in Fig. 10. Upon failure, this contact performs as a surface-to-surface contact with no thickness offsets. Furthermore, after failure, no interface tension is allowed.

3.4. Boundary conditions and loading strategy

Accounting for the symmetry in geometry, support conditions and loading, one-half of the test frame was simulated. As depicted in Figs. 5(a), 6(a) and 7(a) the supports of outer columns were fixed by restraining the three translation degrees of freedom (in the global X, Y and Z directions) of the solid elements of the steel base plate. For the nodes lying on the Y-Z symmetry plane, the symmetry boundary conditions were input. For the middle column at which the actuator load is applied in a displacement-controlled manner, the top nodes were grouped in a set and then the Z-displacement of the node set was controlled to a rate of 100 mm/s in order to match with the loading strategy followed in the experiments (see Figs. 5(a), 6(a) and 7(a)).

4. Calibration of FE models

The test results of the three frames were employed to validate the FE modeling techniques detailed previously. In the following sub-sections, details of the FE results of the three test frames are given.

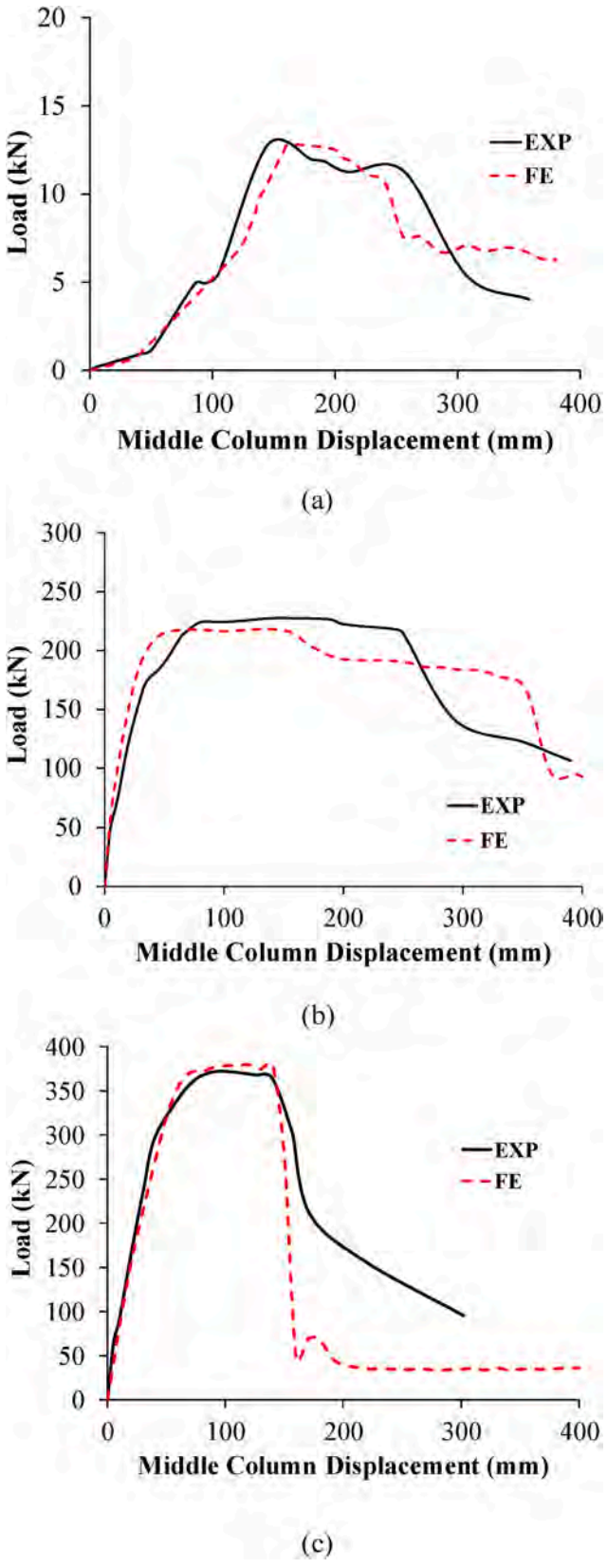

Fig. 14. Comparison of experimental and FE load-displacement envelopes for: (a) Specimen PC-C; (b) Specimen MC-SMF; (c) Specimen PC-S.

4.1. Mode of failure

Experimental modes of failure for the three test specimens are presented in Figs. 11–13. As reported by Al-Salloum et al. [32], behavior of all specimens was almost symmetric during the experiment until ultimate stage and the middle column remained nearly vertical. Upon reaching the ultimate stage, failure of precast specimen PC-C was almost symmetric for the left and right beams and the middle column remained approximately vertical (Fig. 11(a)). However, for other two specimens MC-SMF and PC-S, failure was not symmetric owing to some difference in concrete strength between left and right beams and as a result the middle column could not remain vertical upon failure. In specimen MC-SMF, the left beam had more cracking and concrete crushing than the right one (Fig. 12(a)). However, in frame PC-S, the right beam had a little weaker concrete than the left one, thereby inducing brittle shear failure as seen in Fig. 13(a).

Figs. 11–13 depict comparison of experimentally observed versus numerically predicted modes of failure for test frames PC-C, MC-SMF and PC-S, respectively. The numerically predicted failure modes shown in these figures are represented with the help of maximum principal strain contours at mid-surface of concrete elements. It should be noted that due to modeling one-half of the assembly in the FE analysis, symmetric failure modes were predicted for specimens PC-C, MC-SMF and PC-S as seen in Figs. 11–13. It is clear from the figures that the numerically predicted modes of failure agree well with the experimentally observed ones. Similar to the experiment, the FE analysis predicted an expected hinge behavior for control precast frame PC-C. In the analysis, beams of precast frame PC-C rotated till the inner ends became in touch with the middle column, and the failure of the specimen was because of crushing of the concrete at middle beam-column joint (Fig. 11). The FE mode of failure of the monolithic frame MC-SMF is shown in Fig. 12, which reveals a good match with the experimentally observed one. A plastic hinge was developed in the beam close to the middle joint region as designated by wide flexural cracks along with crushing of concrete in the compression side. Also, at the outer joints, plastic hinges were developed in the beams accompanied with cracking of outer columns adjacent to the connection region. As depicted from Fig. 13, the FE predicted shear failure in the unstrengthened area of beams of specimen PC-S. This failure mode matched well with the experimentally observed shear failure of the right beam shown also in Fig. 13. As discussed by Al-Salloum et al. [32], the reason for having this failure is that addition of steel plates increased substantially both shear and flexural strength of the beams in the area of beam-column joints and the load due to shear strength of the unstrengthened beam section was substantially less than that owing to flexural strength of the upgraded beam section. Similar to the experimental observation, no slippage was predicted at steel plate-to-concrete substrate interface till the end of the analysis time. This may validate the tiebreak contact parameters used in this study.

4.2. Load-displacement response

The numerically predicted load versus middle column displacement envelopes are shown in Fig. 14, as compared with the experimental ones, for the three test frames. As seen in the figures, the FE load-displacement curves match well with the experimental ones, especially for the peak load. As stated earlier, the observed failure mode of precast specimen PC-C was almost symmetric for the left and right beams and as a result, stiffness degradation in the post-peak load stage was approximately the same for both experimental and numerical load-displacement envelopes as seen in Fig. 14(a). However, for other two specimens MC-SMF and PC-S, experimental mode of failure was not symmetric and therefore, the numerically predicted stiffness degradations in the post-peak load stage were higher than the experimental ones as seen in the load-displacement envelopes in Fig. 14(b) and (c).

Table 3 presents the comparison details of the load-displacement response. It is important to note that the ultimate state utilized in

Table 3
Comparison of experimental and FE results for test specimens[a].

Specimen ID	Results	P_u (kN)	$\Delta_{u,c}$(mm)	P_y (kN)	Δ_y(mm)	Δ_u(mm)	μ_Δ	E_u (kN.m)	$\varepsilon_{sb,bot}$(με)[b]	$\varepsilon_{sp,bot}$ (με)[b]
PC-C	EXP	12.8	145	NY	NY	265	–	2.5	74	–
	FE	12.8	160	NY	NY	243	–	2.6	58	–
	EXP/FE	1.00	0.91	–	–	1.09	–	0.97	1.28	–
MC-SMF	EXP	228	144	145	26	269	10.5	59	***95,189***	–
	FE	218	145	153	21	335	16.3	65	***102,065***	–
	EXP/FE	1.04	0.99	0.95	1.25	0.80	0.64	0.90	0.93	–
PC-S	EXP	372	96	315	50	157	3.1	48	1326	***2815***
	FE	379	100	296	45	147	3.2	45	1550	***2924***
	EXP/FE	0.98	0.96	1.07	1.10	1.07	0.97	1.08	0.86	0.96

[a] P_u = peak load; $\Delta_{u,c}$ = middle column displacement at peak load; P_y and Δ_y = load and middle column displacement at first yielding of main beam steel at middle column face (bottom rebars for specimen MC-SMF & bottom edge of steel plates for specimen PC-S); Δ_u = middle column displacement at ultimate state; μ_Δ = displacement ductility = Δ_u/Δ_y; E_u = energy dissipated at ultimate state, $\varepsilon_{sb,bot}$ = peak strain for beam bottom rebars at middle column face; $\varepsilon_{sp,bot}$ = peak strain for bottom edge of steel plates at middle column face, EXP = experimental; FE = finite element; NY = No steel yielding.
[b] Values in italic bold font indicate steel yielding.

Table 3 is taken as that where the peak load decreases by 20% as per Ref. [49]. It is observed from Table 3 that error in the prediction of peak load varies from 0% to 4%. However, as compared with the test results, errors in the prediction of middle column displacement at peak load, middle column displacement at ultimate state, and energy dissipation at ultimate state, respectively, are 1%–9%, 7%–20% and 3%–10%. Also, as depicted from Fig. 14, the stiffness of the test frames was well numerically predicted compared with the experiments. Fig. 14 clearly indicates that the numerical models were efficient in modeling the softening trend, which establishes the precision of the constitutive models. The numerical analysis showed that compared with the monolithic frame MC-SMF, the precast control specimen PC-C had a very high progressive collapse risk due to cutoff of longitudinal beam rebars at beam-to-column connections and then incapability of beams to redistribute the load carried by lost column to adjacent members. The FE analysis also confirmed that although the monolithic frame with continuous beam rebars had considerably higher peak load and energy dissipation as compared to the control precast frame PC-C, the catenary action was not developed owing to: (i) discontinuity of beams at the ends, (ii) insufficient restraint provided by the end columns, (iii) discontinuity of columns due to the consideration of single story, and (iv) absence of column axial load. The FE analysis confirmed the significant peak load enhancement provided by steel plate upgrading technique of frame PC-S, for which the predicted peak load was almost 29.6 and 1.7 times of that for frames PC-C and MC-SMF, respectively. Furthermore, and as seen from Table 3, numerically predicted energy dissipation of strengthened frame PC-S was considerably more than that for control frame PC-C (≈17 times). Yet, numerically predicted energy dissipation and displacement ductility ratio of upgraded frame PC-S were nearly 69% and 20%, in turn, of those for monolithic RC frame MC-SMF.

4.3. Strain gage analysis

Comparisons of experimental and FE load versus rebar strain plots for frames MC-SMF and PC-S are shown in Figs. 15 and 16, respectively. Table 3 presents comparison between experimental and FE peak tensile strain for: (i) bottom steel rebars of beam at middle column face for three test frames, and (ii) steel plates at middle column face of strengthened frame PC-S. As found from Figs. 15 and 16 and Table 3, the numerically obtained steel strains match well with the experimental values. For precast frames PC-C and PC-S, the peak strains for bottom steel rebars of beam at middle column face were considerably less than the yield strain because of the discontinuity of these rebars at the joint region. Yet, for monolithic frame MC-SMF, all tension steel rebars (at beam ends and at outer columns close to the joint region) had strains significantly higher than the yield value (see Fig. 15 and Table 3), which verified the development of plastic hinges at the beam ends as mentioned earlier. For strengthened frame PC-S, tensile strain of the lowest edge of steel plate at face of middle column was about 1.4 times the yield value (Table 3 and Fig. 16). However, tensile strains at the top edge of steel plates at face of outer columns were less than the yield value as seen in Fig. 16(b). It is therefore revealed that neither of the strengthened sections of beams of frame PC-S attained its ultimate flexural strength owing to brittle shear failure of the unstrengthened portion of the beam (Fig. 13) and detailed in Refs. [32]. Nevertheless, because of the high peak load taken by frame PC-S, its outer columns attained their flexural strength at the end of the experiment (or analysis time) by having high tensile strains (≈20,000 με) for outer rebars close to joint region (Fig. 16(c)).

5. Effect of strengthening plate parameters

The calibrated FE models were extended to investigate the impact of different steel plate parameters on the behavior of strengthened precast RC frames due to middle column-missing event. The FE matrix consisted of 26 specimens with different steel plate parameters such as: plate thickness, steel grade, and anchorage condition within the compression zone (see Table 4). Since both experimental and FE analysis demonstrated that specimen PC-S failed suddenly due to shear failure of unstrengthened beam portion as a result of steel plate overdesign, different plate thicknesses with two steel grades were investigated. As seen in Table 4, six plate thicknesses ranging from 3 to 8 mm were studied for ASTM A572 G50 steel; however, for ASTM A36 steel, seven plate thicknesses varying from 3 to 10 mm were investigated. As per the details given earlier for strengthened specimen PC-S in Fig. 3, steel plates near beam-column connections were not properly restrained by threaded rods, especially against plate buckling in the compression zone. This was not critical for specimen PC-S due to the large plate thickness of 10 mm, for which the section did not reach its full flexural capacity due to abrupt shear failure as outlined before. However, for smaller thicknesses, this may be of big concern. Therefore, two anchorage conditions were numerically investigated for each thickness. The first was to study the performance with threaded rods layout as given for specimen PC-S (Fig. 3). This case is considered without steel plate anchorage within the compression zone (see Table 4: specimens PC-S-3-A36 to PC-S-10-A36 & PC-S-3-A572 to PC-S-8-A572). The second case was to investigate the behavior with new layout of threaded rods, which were designed to have fully anchored steel plates as depicted from Fig. 17 (see Table 4: specimens PC-S-3-A36-FA to PC-S-10-A36-FA & PC-S-3-A572-FA to PC-S-8-A572-FA).

It should be noted here that in the design of threaded rods for provision of full anchorage, simple calculations were used in which elastic Euler buckling was taken for steel plates in the compression side of the beam section. These plates may perform as axially loaded columns in compression. Steel plate between rods was assumed to perform as a fixed-fixed column. Therefore, the maximum center-to-center spacing

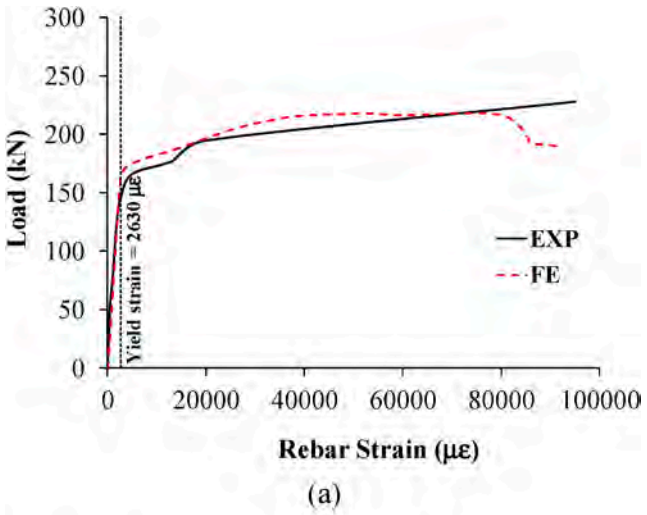

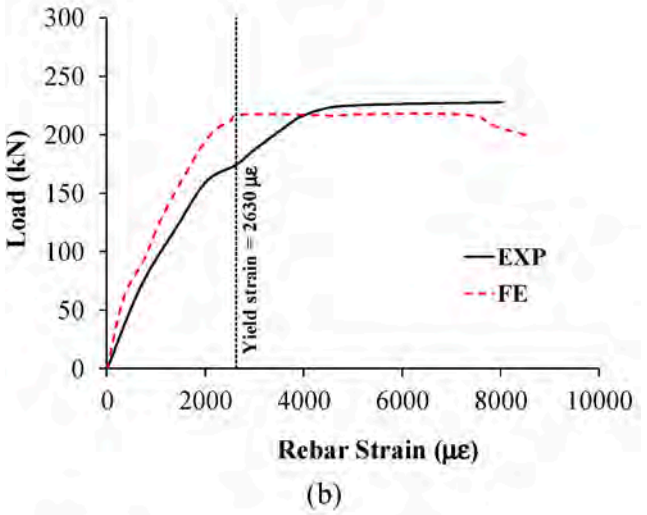

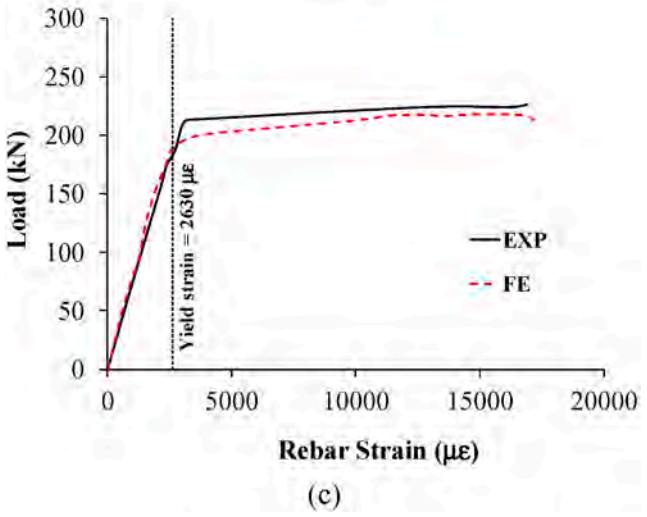

Fig. 15. Comparison of experimental and FE load vs. rebar strain curves for specimen MC-SMF: (a) Bottom rebars of beam at face of middle column; (b) Top rebars of beam at face of outer column; (c) Outer rebars of exterior column near connection zone.

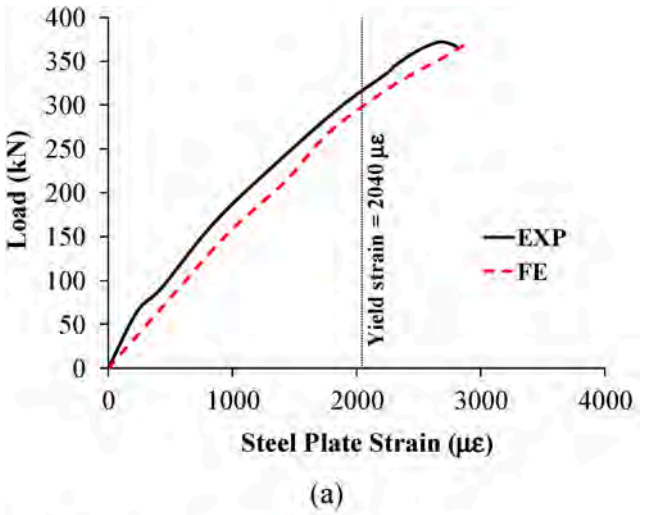

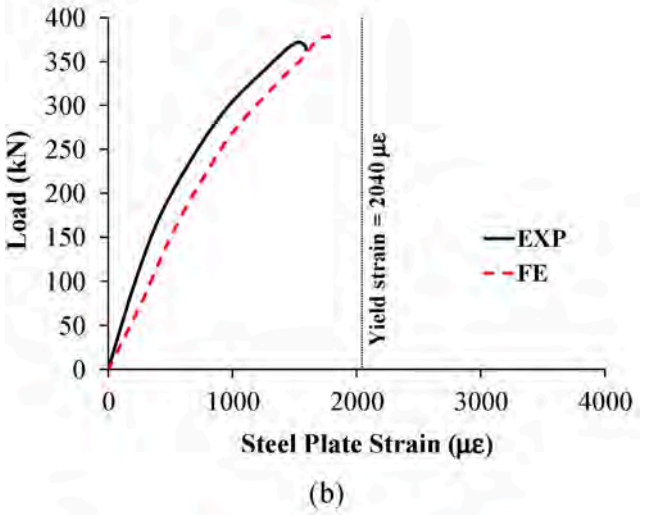

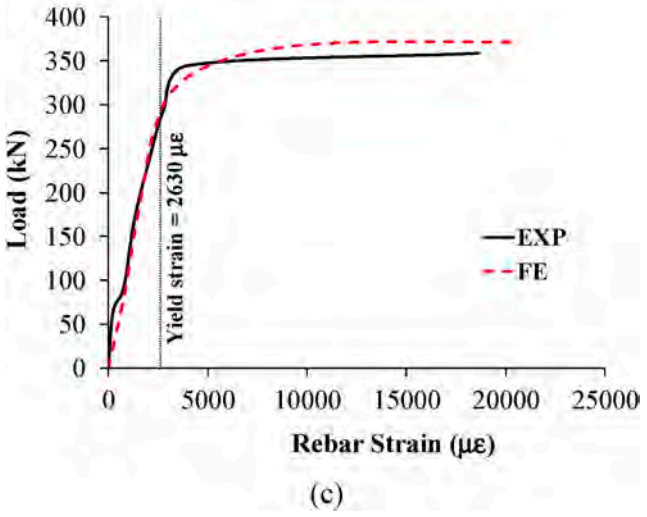

Fig. 16. Comparison of experimental and FE load vs. steel strain curves for specimen PC-S: (a) Bottom edge of steel plate at face of middle column; (b) Top edge of steel plate at face of outer column; (c) Outer rebars of exterior column near connection zone.

Table 4
Details and FE results of specimens used in the parametric study*.

Specimen ID	Steel plate strengthening scheme			FE results							
	t_p (mm)	Grade	Anchorage within compression zone	P_y (kN)	P_u (kN)	Δ_y (mm)	Δ_u (mm)	μ_Δ	E_u (kN.m)	$\varepsilon_{sp,bot}$ (με)	Failure mode
PC-S-3-A36	3	A36	NO	31	188	5	192	35.5	31	97,771	FF(Y-CC-BKL)
PC-S-3-A36-FA	3	A36	YES	41	193	7	166	24.0	27	199,179	FF(FR-CC)
PC-S-4-A36	4	A36	NO	44	230	8	232	30.7	46	85,192	FF(Y-CC-BKL)
PC-S-4-A36-FA	4	A36	YES	61	242	10	201	20.6	42	232,883	FF(FR-CC)
PC-S-5-A36	5	A36	NO	65	271	11	262	24.5	62	84,696	FF(Y-CC-BKL)
PC-S-5-A36-FA	5	A36	YES	76	286	12	227	18.8	56	261,229	FF(FR-CC)
PC-S-6-A36	6	A36	NO	81	312	12	261	21.2	70	76,955	FF(Y-CC-BKL)
PC-S-6-A36-FA	6	A36	YES	93	328	14	282	20.4	79	262,718	FF(FR-CC)
PC-S-7-A36	7	A36	NO	97	337	14	301	21.3	89	77,425	FF(Y-CC-BKL)
PC-S-7-A36-FA	7	A36	YES	123	355	17	283	16.5	86	274,527	FF(FR-CC)
PC-S-8-A36	8	A36	NO	138	358	19	265	14.0	83	66,086	FF(Y-CC)
PC-S-8-A36-FA	8	A36	YES	137	370	19	287	15.4	93	278,204	FF(Y-CC)
PC-S-10-A36	10	A36	NO	167	381	22	162	7.3	50	9334	SF
PC-S-10-A36-FA	10	A36	YES	169	376	22	172	7.8	54	18,940	SF
PC-S-3-A572	3	A572 GR50	NO	78	263	13	206	15.3	45	80,757	FF(Y-CC-BKL)
PC-S-3-A572-FA	3	A572 GR50	YES	82	269	14	166	12.0	36	192,584	FF(FR-CC)
PC-S-4-A572	4	A572 GR50	NO	130	323	21	230	12.8	63	66,943	FF(Y-CC-BKL)
PC-S-4-A572-FA	4	A572 GR50	YES	129	329	20	217	10.6	59	238,979	FF(FR-CC)
PC-S-5-A572	5	A572 GR50	NO	157	356	24	252	10.3	76	63,426	FF(Y-CC-BKL)
PC-S-5-A572-FA	5	A572 GR50	YES	159	368	25	265	10.7	81	235,746	FF(FR-CC)
PC-S-6-A572	6	A572 GR50	NO	201	373	31	163	5.3	48	13,346	SF
PC-S-6-A572-FA	6	A572 GR50	YES	197	376	31	172	5.6	52	29,939	SF
PC-S-7-A572	7	A572 GR50	NO	215	373	33	152	4.6	45	6892	SF
PC-S-7-A572-FA	7	A572 GR50	YES	217	377	33	163	4.9	49	12,109	SF
PC-S-8-A572	8	A572 GR50	NO	239	375	37	162	4.4	49	5331	SF
PC-S-8-A572-FA	8	A572 GR50	YES	250	373	38	143	3.7	42	7566	SF

* t_p = thickness of steel plate per side of beam; P_y = load at first yielding of bottom edge of steel plates at middle column face; P_u = peak load; Δ_y = middle column displacement at first yielding of bottom edge of steel plates at middle column face; Δ_u = middle column displacement at ultimate state; μ_Δ = displacement ductility = Δ_u/Δ_y; E_u = energy dissipated at ultimate state; $\varepsilon_{sp,bot}$ = peak strain for bottom edge of steel plates at middle column face; FF = flexural failure of beam at middle column face; FF(Y-CC-BKL) = flexural failure of beam at middle column face, initiated by yielding at bottom edge of steel plates followed by crushing of compression concrete and infill grout at column interface and ending up with buckling of steel plates in the compression zone; FF(FR-CC) = flexural failure of beam at middle column face, initiated by fracture of steel plates followed by crushing of compression concrete and infill grout at column interface; FF(Y-CC) = flexural failure of beam at middle column face, initiated by yielding at bottom edge of steel plates followed by crushing of compression concrete and infill grout at column interface; SF = shear failure of unstrengthened portion of beam.

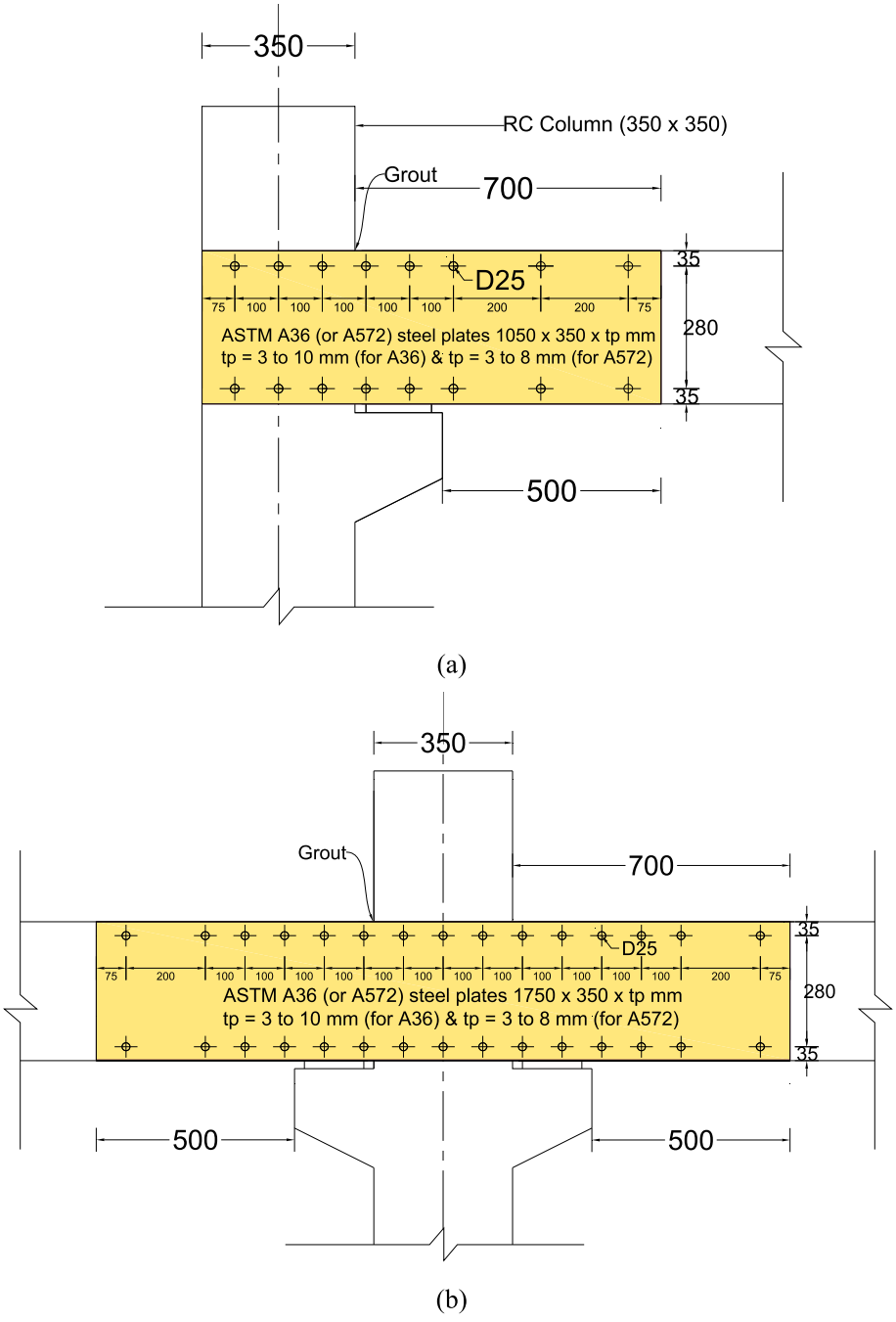

Fig. 17. Anchorage details for strengthened specimens PC-S-3-A36-FA to PC-S-10-A36-FA & PC-S-3-A572-FA to PC-S-8-A572-FA (Note: All dimensions are in mm): (a) Outer connection zone; (b) Middle connection zone.

between rods that could inhibit buckling of steel plates in the compression zone of the beam was approximately calculated by equating the Euler buckling stress to the yield strength of the plate according to the following formula.

$$s_{\max} = 2\pi t_p \sqrt{\frac{E_s}{12 f_{yp}}} \tag{16}$$

where t_p = thickness of steel plate; E_s = modulus of elasticity of steel (taken as 2×10^5 MPa); f_{yp} = yield strength of plate. The design of anchorage details shown in Fig. 17 was based on ASTM A572 G50 steel plates with 3 mm thickness, and it was conservatively assumed for all other specimens with full anchorage. It should be noted that in the analysis of specimens listed in Table 4, the material properties of specimen PC-S was utilized, except A36 steel grade for which the yield and ultimate strengths were assumed as 248 and 400 MPa, respectively.

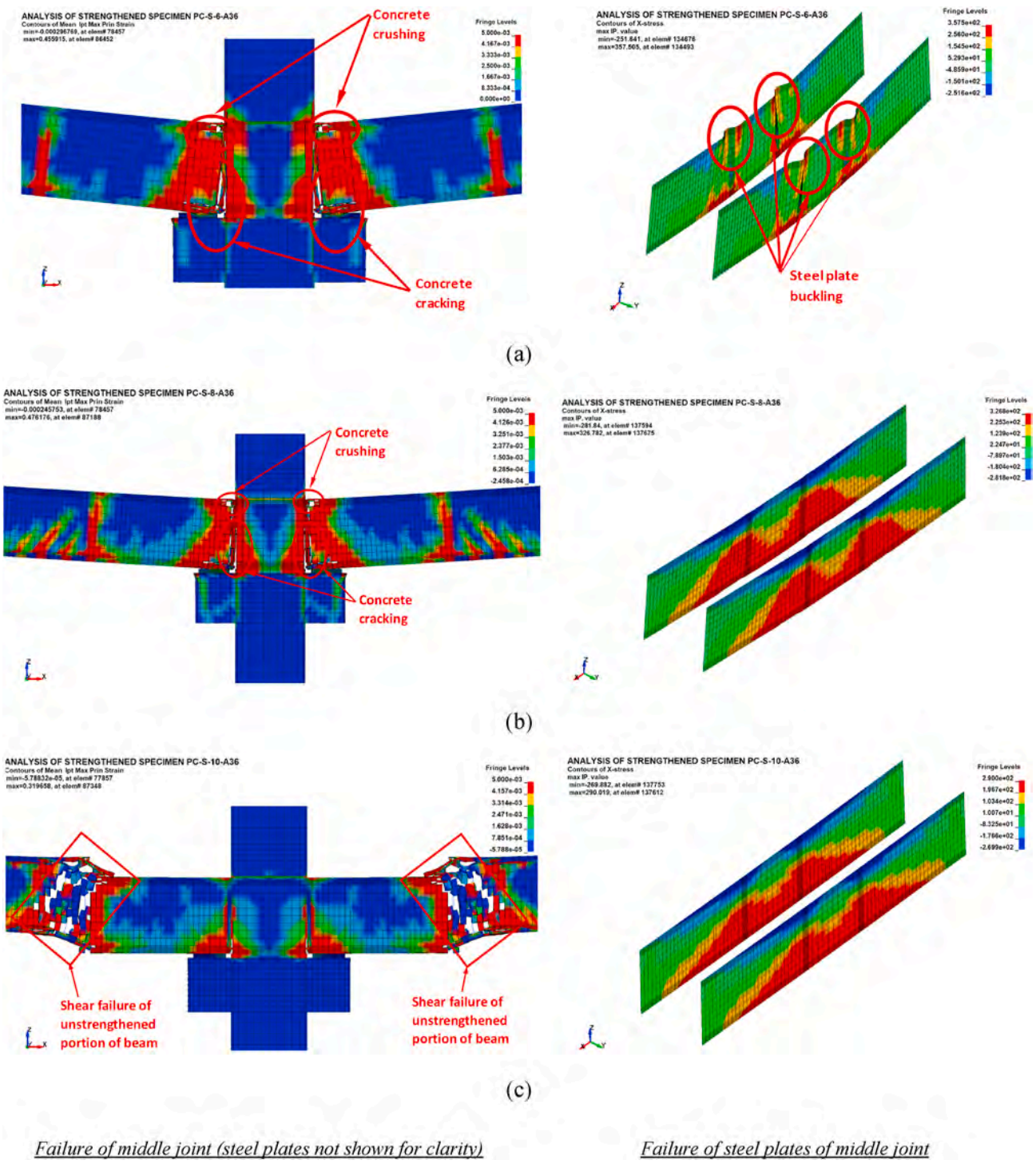

Fig. 18. FE mode of failure for representative strengthened specimens without anchorage within the compression zone: (a) PC-S-6-A36; (b) PC-S-8-A36; (c) PC-S-10-A36.

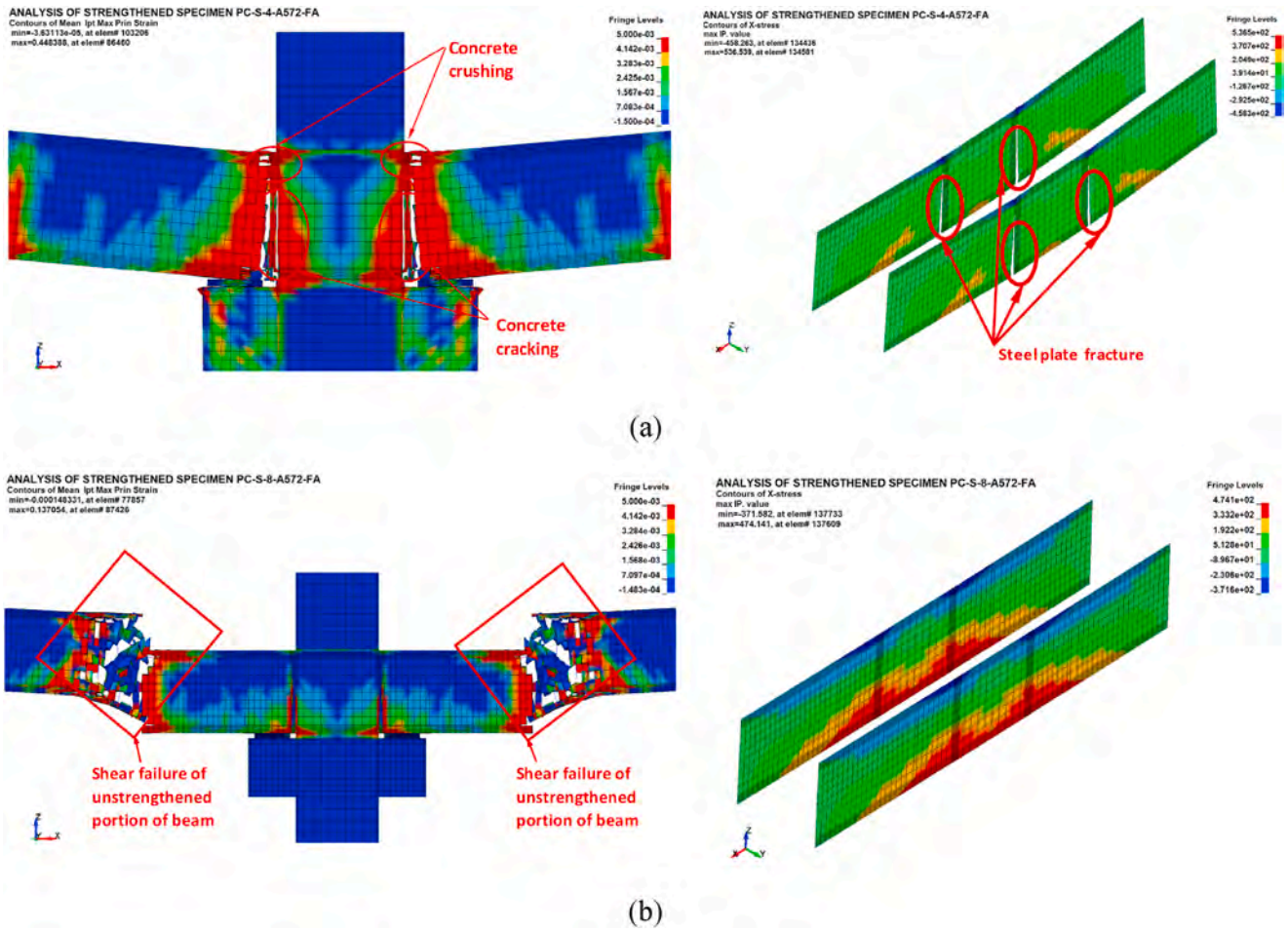

Fig. 19. FE mode of failure for representative strengthened specimens with full anchorage within the compression zone: (a) PC-S-4-A572-FA; (b) PC-S-8-A572-FA.

Table 4 presents a summary of the numerical results of the 26 specimens employed in the parametric study. The numerically predicted mode of failure for representative strengthened frames without anchorage within the compression zone are displayed in Fig. 18. For plates with thickness not exceeding 5 mm for A572 steel (or 7 mm for A36 steel), flexural failure of beams at middle column face was predicted. This failure commenced with yielding at bottom edge of steel plates followed by crushing of compression concrete and infill grout at column interface and ended up with buckling of steel plates in the compression zone, as shown in Fig. 18(a) for frame PC-S-6-A36. For the same case of no compression zone anchorage, buckling of plates was not predicted for larger thicknesses. For A36 steel, flexural failure due to yielding of plate followed by crushing of compression concrete and infill grout at middle column face was found for plate thickness of 8 mm (see Fig. 18(b)). However, for 10 mm thick plate, beam shear failure was predicted as seen in Fig. 18(c). For A572 steel, shear failure of unstrengthened portion of beam was noticed for plate thicknesses exceeding 5 mm. It should be noted that for A36 specimens with large plate thickness of 8 mm, possibility of buckling is significantly reduced and hence effect of anchorage is not significant as seen from Table 4. Failure of specimens PC-S-8-A36 and PC-S-8-A36-FA was identical (yielding of steel plate followed by concrete crushing) and the difference in the peak load was insignificant (≈3%).

FE mode of failure for representative strengthened frames with full anchorage within the compression zone are shown in Fig. 19. For the case of fully anchored plates with maximum thickness of 5 and 7 mm for A572 and A36 steel, respectively, flexural failure of beam at middle column face was predicted. This failure was initiated by fracture of plates followed by crushing of the compression concrete and infill grout at column face as illustrated in Fig. 19(a) for specimen PC-S-4-A572-FA. For larger plate thicknesses, either flexural failure due to yielding of plate followed by crushing of the compression zone (case of A36 steel with 8 mm thick plate) or brittle shear failure of unstrengthened portion of beam (A36 steel with 10 mm thick plate or A572 steel with 6–8 mm thick plates) occurred as displayed in Fig. 19(b).

Load-displacement envelopes for representative samples of studied frames are shown in Fig. 20. Load-displacement envelope for monolithic frame MC-SMF is also shown in Fig. 20 for the sake of comparison. Except for specimens failing by shear, both specimens having A36 steel plates with thickness of 4 mm or more and specimens with A572 steel plates have acceptable load-displacement characteristics up to middle column displacement of 200 mm (see Fig. 20).

In order to help in assessing the effectiveness of steel plate strengthening technique in enhancing the response of precast concrete beam-to-column joints under column missing event, two new parameters were proposed in this paper: (i) the peak load efficiency (η_p) and (ii) the energy efficiency (η_E). They can be calculated from the following equations.

$$\eta_p = \frac{P_{u,p}}{P_{u,m}} \times 100\% \tag{17}$$

$$\eta_E = \frac{E_{u,p}}{E_{u,m}} \times 100\% \tag{18}$$

where $P_{u,p}$ = ultimate load of steel-plated precast RC frame; $P_{u,m}$ = ultimate load of equivalent monolithic RC frame having continuous longitudinal beam rebars (frame MC-SMF); $E_{u,p}$ = energy dissipation for

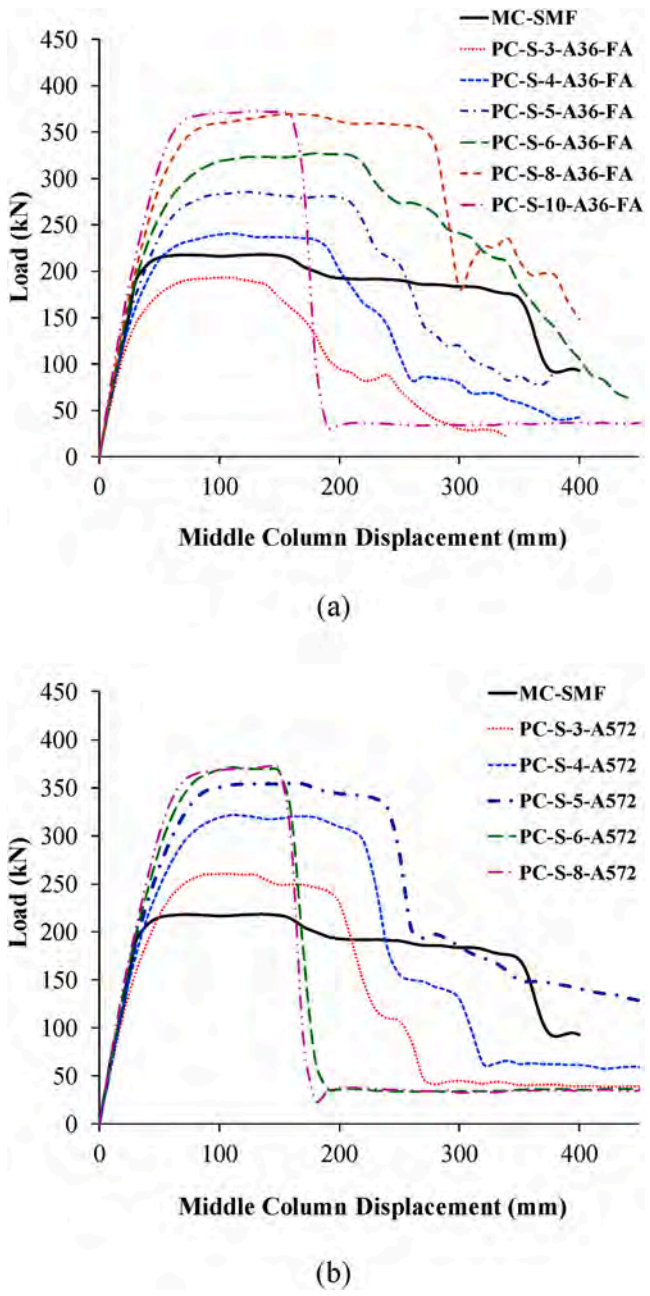

Fig. 20. Load-displacement envelopes for representative strengthened specimens used in the parametric study (based on FE analysis): (a) A36 specimens with fully anchored plates; (b) A572 specimens without fully anchored plates.

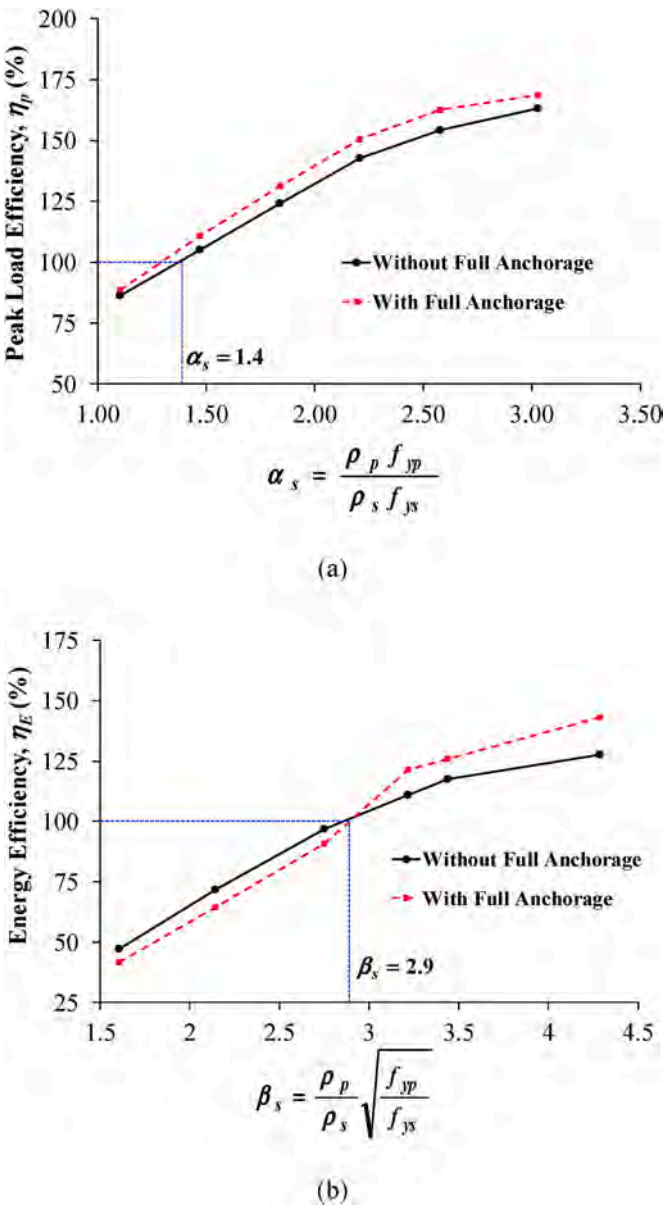

Fig. 21. Effect of strengthening parameters α_s and β_s on efficiency of precast specimens under column-removal scenario (based on FE analysis): (a); (b).

steel-plated precast RC frame at ultimate state; and $E_{u,m}$ = energy dissipation for equivalent monolithic RC frame having continuous beam rebars (frame MC-SMF). Another two new plate strengthening parameters α_s and β_s were also introduced in this research. These parameters are given by

$$\alpha_s = \frac{\rho_p f_{yp}}{\rho_s f_{ys}} \tag{19}$$

$$\beta_s = \frac{\rho_p}{\rho_s}\sqrt{\frac{f_{yp}}{f_{ys}}} \tag{20}$$

where ρ_p = steel plate ratio calculated as the ratio of cross-sectional area of steel plates to total area of concrete section; f_{yp} = static yield strength of steel plates; ρ_s = ratio of beam bottom rebars and f_{ys} = static yield strength of beam bottom rebars. The peak load and energy efficiencies were calculated for strengthened specimens of Table 4 failing by flexure (18 specimens) and are then plotted versus strengthening parameters α_s and β_s as presented in Fig. 21(a) and (b), respectively.

It is indicated from Fig. 21(a) and (b) that the difference between both peak load and energy efficiencies for the two cases of plate anchorage is insignificant for all range of strengthening parameters α_s and β_s. It is also found from the FE results shown in Table 4 that even for the case of without full anchorage, buckling of plates was postponed until crushing of concrete in the compression zone at higher stages of beam deformation. Hence, in order to save construction time and costs associated with the difficulty of installing the threaded rods for plate-to-concrete anchorage, it is recommended to provide plate anchorage within the compression zone using the minimum number of rods with maximum spacing of $8d_b$ in the horizontal direction, where d_b is the rod diameter. This may help to alleviate or even postpone buckling of thin plates until stages of large beam deformation. The edge distance of rods is recommended as $3d_b$; however, for outer beam-column connections, the edge distance of rods measured to the outer edge of the exterior

column should not be less than 100 mm for practical considerations. In order to achieve 100% peak load efficiency, the strengthening parameter α_s should not be less than 1.4; yet, for an energy efficiency of 100%, the strengthening parameter β_s should not be less than 2.9.

6. Conclusions

The key outcomes of this paper can be listed as follows:

1. The investigated type of precast RC beam-column joint had a very high progressive collapse risk because of discontinuity in the longitudinal rebars of beams at beam-column connection regions and therefore incapability of beams to redistribute the load carried by failed column to adjacent members.
2. Although the monolithic RC frame with continuity in beam rebars had significantly higher ultimate load and energy dissipation compared to existing precast frame PC-C, the development of catenary action was inhibited due to: discontinuity of beams beyond the exterior columns and the insufficient restraint provided by outer columns.
3. Upgrading of precast RC beam-column joints with bolted steel plates was efficient in increasing the peak load (about 29 times of precast frame PC-C) and energy dissipation of the frame assembly. However, special attention has to be paid to the steel plate parameters (grade and thickness). Increasing the thickness and/or grade of steel plates may increase the flexural capacity of the beam significantly so that it will exceed the shear capacity of its unstrengthened part and hence may induce brittle shear failure.
4. The FE analysis conducted in this work was found relevant in assessing the behavior of monolithic and precast RC frames under column-loss event. Thus, this analysis may be employed in forthcoming work to study the progressive collapse risk of different types of precast RC beam-column joints.
5. Two sets of parameters were proposed in this research. The first set includes peak load and energy efficiency parameters (η_p & η_E); whereas the other set comprises plate strengthening parameters α_s and β_s. They were used in comparing response of strengthened precast RC frames with corresponding monolithic RC frame. For 100% peak load efficiency, the strengthening parameter α_s should not be less than 1.4; yet, for an energy efficiency of 100%, the strengthening parameter β_s should not be less than 2.9.
6. In order to alleviate or postpone buckling of thin steel plates until stages of large beam deformation, it is recommended to provide plate anchorage within the compression zone of the beams using rods with maximum center-to-center spacing of $8d_b$ in the horizontal direction (d_b is the rod diameter). The edge distance of rods is recommended as $3d_b$; however, for outer joints, the edge distance of rods measured to the outer edge of the exterior column should not be less than 100 mm for practical considerations.

CRediT authorship contribution statement

Hussein M. Elsanadedy: Conceptualization, Methodology, Writing - original draft. **Yousef A. Al-Salloum:** Supervision, Project administration, Funding acquisition. **Mohammed A. Alrubaidi:** Validation, Writing - review & editing. **Tarek H. Almusallam:** Visualization, Writing - review & editing. **Husain Abbas:** Writing - review & editing.

Declaration of competing interest

The authors declare that they have no known competing financial interests or personal relationships that could have appeared to influence the work reported in this paper.

Acknowledgements

The authors are grateful to the Deanship of Scientific Research, King Saud University, for funding through Vice Deanship of Scientific Research Chairs.

References

[1] B.J. Smith, Y.C. Kurama, M.J. McGinnis, Behavior of precast concrete shear walls for seismic regions: comparison of hybrid and emulative specimens, J. Struct. Eng-ASCE 139 (11) (2013) 1917–1927.
[2] Y. Chen, Q. Zhang, J. Feng, Z. Zhang, Experimental study on shear resistance of precast RC shear walls with novel bundled connections, J. Earthq. Tsunami 13 (3n04) (2019), 1940002.
[3] H.K. Choi, Y.C. Choi, C.S. Choi, Development and testing of precast concrete beam-to-column connections, Eng. Struct. 56 (2013) 1820–1835.
[4] R. Vidjeapriya, K.P. Jaya, Experimental study on two simple mechanical precast beam column connections under reverse cyclic loading, J. Perform. Constr. Facil. 27 (2013) 402–414.
[5] O. Ertas, S. Ozden, T. Ozturan, Ductile connections in precast concrete moment resisting frames, PCI J. 5 (2006) 2–12.
[6] M.K. Joshi, C.V. Murty, M.P. Jaisingh, Cyclic behaviour of precast RC connections, Indian Concr. J. 79 (2005) 43–50.
[7] H.M. Elsanadedy, T.H. Almusallam, Y.A. Al-Salloum, H. Abbas, Investigation of precast RC beam-column assemblies under column-loss scenario, Construct. Build. Mater. 142 (2017) 552–571.
[8] L.F. Maya, C. Zanuy, L. Albajar, C. Lopez, J. Portabella, Experimental assessment of connections for precast concrete frames using ultra high performance fibre reinforced concrete, Construct. Build. Mater. 48 (2013) 173–186.
[9] G. Magliulo, M. Ercolino, M. Cimmino, V. Capozzi, G. Manfredi, FEM analysis of the strength of RC beam-to-column dowel connections under monotonic actions, Construct. Build. Mater. 69 (2014) 271–284.
[10] Y. Chen, J. Yan, P. Sareh, J. Feng, Feasible prestress modes for cable-strut structures with multiple self-stress states using particle swarm optimization, J. Comput. Civ. Eng. 34 (3) (2020), 04020003.
[11] A. Caporale, L. Feo, R. Luciano, R. Penna, Numerical collapse load of multi-span masonry arch structures with FRP reinforcement, Compos. B Eng. 54 (2013) 71–84.
[12] D.E. Allen, W.R. Schriever, Progressive Collapse, Abnormal Load, and Building Codes, Structural Failure: Modes, Causes, Responsibilities, Proc. American Society of Civil Engineers, New York, USA, 1972.
[13] T.H. Almusallam, H.M. Elsanadedy, H. Abbas, S.H. Alsayed, Y.A. Al-Salloum, Progressive collapse analysis of a RC building subjected to blast loads, Int. J. Struct. Eng. Mech. 36 (3) (2010) 301–319.
[14] T. Almusallam, Y. Al-Salloum, T. Ngo, P. Mendis, H. Abbas, Experimental investigation of progressive collapse potential of ordinary and special moment-resisting reinforced concrete frames, Mater. Struct. 50 (2017) 137.
[15] H.M. Elsanadedy, T.H. Almusallam, Y.R. Alharbi, Y.A. Al-Salloum, H. Abbas, Progressive collapse potential of a typical steel building due to blast attacks, J. Constr. Steel Res. 101 (2014) 143–157.
[16] J. Choi, D. Chang, Prevention of progressive collapse for building structures to member disappearance by accidental actions, J. Loss Prevent. Proc. 22 (2009) 1016–1019.
[17] Y.A. Al-Salloum, T.H. Almusallam, M.Y. Khawaji, T. Ngo, H.M. Elsanadedy, H. Abbas, Progressive collapse analysis of RC buildings against internal blast, Adv. Struct. Eng. 18 (12) (2015) 2181–2192.
[18] P.X. Dat, T.K. Haiand, Y. Jun, A simplified approach to assess progressive collapse resistance of reinforced concrete framed structures, Eng. Struct. 101 (2015) 45–57.
[19] Y. Bao, S.K. Kunnath, S. El-Tawil, H.S. Lew, Macromodel-based simulation of progressive collapse: RC frame structures, J. Struct. Eng-ASCE 134 (7) (2008) 1079–1091.
[20] S.B. Kang, K.H. Tan, Behaviour of precast concrete beam-column sub–assemblages subject to column removal, Eng. Struct. 93 (2015) 85–96.
[21] I. Azim, J. Yang, S. Bhatta, F. Wang, Q-f. Liu, Factors influencing the progressive collapse resistance of RC frame structures, J. Build. Eng. 27 (2020), 100986.
[22] Y.-H. Weng, K. Qian, F. Fu, Q. Fang, Numerical investigation on load redistribution capacity of flat slab substructures to resist progressive collapse, J. Build. Eng. 29 (2020), 101109.
[23] Y. Bai, S. Guan, X. Lin, B. Mou, Seismic collapse analysis of high-rise reinforced concrete frames under long-period ground motions, Struct. Des. Tall Spec. 28 (1) (2019) e1566.
[24] S.M. Alcocer, J.O. Jirsa, Strength of reinforced concrete frame connections rehabilitated by jacketing, ACI Struct. J. 90 (3) (1993) 249–261.
[25] A. Ghobarah, T.S. Aziz, A. Biddah, Rehabilitation of reinforced concrete frame connections using corrugated steel jacketing, ACI Struct. J. 94 (3) (1997) 282–294.
[26] C. Antonopoulos, T.C. Triantafillou, Experimental investigation of FRP-strengthened RC beam-column joints, J. Compos. Constr. ASCE 7 (1) (2003) 39–49.
[27] Y.A. Al-Salloum, T.H. Almusallam, Seismic response of interior beam-column joints upgraded with FRP sheets. I: experimental study, J. Compos. Constr. ASCE 11 (6) (2007) 575–589.
[28] S.H. Alsayed, Y.A. Al-Salloum, T.H. Almusallam, N.A. Siddiqui, Seismic response of FRP-upgraded exterior RC beam-column joints, J. Compos. Constr. ASCE 14 (2) (2010) 195–208.

[29] Y.A. Al-Salloum, N.A. Siddiqui, H.M. Elsanadedy, A.A. Abadel, M.A. Aqel, Textile-reinforced mortar versus FRP as strengthening material for seismically deficient RC beam-column joints, J. Compos. Constr. ASCE 15 (6) (2011) 920–933.
[30] T. Da Fonseca, S.F. de Almeida, J.B. de Hanai, L. Ye, P. Feng, Q. Yue, Beam-to-column connection of a precast concrete frame strengthened by NSM CFRP strips. Advances in FRP Composites in Civil Engineering, Springer, 2011, https://doi.org/10.1007/978-3-642-17487-2_189.
[31] J. Pan, A. Wang, F. Wu, Strengthening of precast RC frame to mitigate progressive collapse by externally bonded CFRP sheets anchored with HFRP anchors, Adv. Civ. Eng. 2018 (2018) 1–11, 8098242.
[32] Y.A. Al-Salloum, M.A. Alrubaidi, H.M. Elsanadedy, T.H. Almusallam, R.A. Iqbal, Strengthening of precast RC beam-column connections for progressive collapse mitigation using bolted steel plates, Eng. Struct. 161 (2018) 146–160.
[33] Livermore Software Technology Corporation (LSTC), LS-DYNA User's Keyword Manual (Nonlinear Dynamic Analysis of Structures in Three Dimensions), vol. 1, LSTC, Livermore, CA, 2007. Version 971.
[34] ACI Committee 318, Building Code Requirements for Structural Concrete and Commentary, ACI, vols. 318–19, American Concrete Institute, Detroit, MI, USA, 2019.
[35] American Society for Testing and Materials (ASTM), Standard Test Method for Compressive Strength of Cylindrical Concrete Specimens, ASTM C39/C39M, West Conshohocken, PA, USA, 2010.
[36] American Society for Testing and Materials (ASTM), Standard Test Methods for Tension Testing of Metallic Materials, ASTM E8/E8M, West Conshohocken, PA, USA, 2009.
[37] ASTM, Standard Test Methods and Definitions for Mechanical Testing of Steel Products, American Society for Testing and Materials, West Conshohocken, PA, USA, 2016. ASTM A370 - 16.
[38] T.B. Belytschko, C.S. Tsay, Explicit algorithms for non-linear dynamics of shells, J. Appl. Mech. Applied Mechanics Division, ASME 48 (1981) 209–231.
[39] H.M. Elsanadedy, Y.A. Al-Salloum, T.H. Almusallam, T. Ngo, H. Abbas, Assessment of progressive collapse potential of special moment resisting RC frames–Experimental and FE study, Eng. Fail. Anal. 105 (2019) 896–918.
[40] H.M. Elsanadedy, T.H. Almusallam, S.H. Alsayed, Y.A. Al-Salloum, Flexural strengthening of RC beams using textile reinforced mortar – experimental and numerical study, Compos. Struct. 97 (2013) 40–55.
[41] H.M. Elsanadedy, Y.A. Al-Salloum, T.H. Almusallam, A.O. Alshenawy, H. Abbas, Experimental and numerical study on FRP-upgraded RC beams with large rectangular web openings in shear zones, Construct. Build. Mater. 194 (2019) 322–343.
[42] H.M. Elsanadedy, T.H. Almusallam, S.H. Alsayed, Y.A. Al-Salloum, Experimental and FE study on RC one-way slabs upgraded with FRP composites, KSCE J. Civ. Eng. 19 (4) (2015) 1024–1040.
[43] T.H. Almusallam, Y.A. Al-Salloum, H.M. Elsanadedy, A.O. Alshenawy, R.A. Iqbal, Behavior of FRP-strengthened RC beams with large rectangular web openings in flexure zones – experimental and numerical study, Int. J. Concr. Struct. M. 12 (2018) 47, 28pp.
[44] T.H. Almusallam, H.M. Elsanadedy, Y.A. Al-Salloum, Effect of longitudinal steel ratio on behavior of RC beams strengthened with FRP composites – experimental and FE study, J. Compos. Constr. ASCE 19 (1) (2015).
[45] Y.D. Murray, A. Abu-Odeh, R. Bligh, Evaluation of Concrete Material Model 159, Report No. FHWA-HRT-05-063, US Department of Transportation, Federal Highway Administration National Transportation Systems Center, USA, 2007.
[46] R.M. Christensen, A nonlinear theory of viscoelasticity for application to elastomers, J. Appl. Mech. Applied Mechanics Division, ASME 47 (1980) 762–768.
[47] California Department of Transportation (Caltrans), Memo to Designers 7-1 (Bridge Bearings), 1994, 69pp., June.
[48] J. Silfwerbrand, Shear bond strength in repaired concrete structures, Mater. Struct. 36 (2003) 419–424.
[49] New Zealand Standard (NZS), Code of Practice for General Structural Design and Design Loadings for Buildings 1, NZS 4203, 1992. New Zealand.